Published in final edited form as:

*Nat Struct Mol Biol*. 2020 July ; 27(7): 635–644. doi:10.1038/s41594-020-0428-2.

# Gating of human TRPV3 in a lipid bilayer

**Zengqin Deng**[1,2,8], **Grigory Maksaev**[1,2,8], **Michael Rau**[3], **Zili Xie**[4,5], **Hongzhen Hu**[4,5], **James A.J. Fitzpatrick**[1,3,6,7], **Peng Yuan**[1,2,*]

[1]Department of Cell Biology and Physiology, Washington University School of Medicine, Saint Louis, Missouri, USA

[2]Center for the Investigation of Membrane Excitability Diseases, Washington University School of Medicine, Saint Louis, Missouri, USA

[3]Washington University Center for Cellular Imaging, Washington University School of Medicine, Saint Louis, Missouri, USA

[4]Department of Anesthesiology, Washington University School of Medicine, Saint Louis, Missouri, USA

[5]Center for the Study of Itch, Washington University School of Medicine, Saint Louis, Missouri, USA

[6]Department of Neuroscience, Washington University School of Medicine, Saint Louis, Missouri, USA

[7]Department of Biomedical Engineering, Washington University in Saint Louis, Saint Louis, Missouri, USA

[8]These authors contributed equally to this work

## Abstract

The TRPV3 channel plays a critical role in skin physiology, and mutations in TRPV3 result in the development of a congenital skin disorder, Olmsted syndrome. Here we describe multiple cryo-electron microscopy structures of human TRPV3 reconstituted into lipid nanodiscs, representing distinct functional states during the gating cycle. The ligand-free, closed conformation reveals well-ordered lipids interacting with the channel and two physical constrictions along the ion conduction pore involving both the extracellular selectivity filter and intracellular helix bundle crossing. Both the selectivity filter and bundle crossing expand upon activation, accompanied by substantial structural rearrangements at the cytoplasmic inter-subunit interface. Transition to the inactivated state involves a secondary structure change of the pore-lining helix, which contains a



*Correspondence should be addressed to P.Y. (yuanp@wustl.edu).

Author Contributions

Z.D. performed biochemical preparations, cryo-EM experiments, structural determination and analysis. G.M. conducted electrophysiology experiments. M.R. and J.A.J.F. performed cryo-EM data acquisition in conjunction with Z.D. Z.X. and H.H. helped with functional studies. P.Y. designed and supervised the project. Z.D., G.M., and P.Y. analyzed the results and prepared the manuscript with input from all authors.

Competing Interests

The authors declare no competing interests.

π-helical segment in the closed and open conformations but becomes entirely α-helical upon inactivation. Together with electrophysiological characterization, structures of TRPV3 in a lipid membrane environment provide unique insights into channel activation and inactivation mechanisms.

**Keywords**

Membrane proteins; Ion channels; TRP channels; TRPV3; Cryo-electron microscopy

## Introduction

Transient receptor potential (TRP) channels are polymodal sensors that convert a multitude of environmental cues into cellular signaling events essential for physiology[1]. The vanilloid subfamily (TRPV) comprises six members (TRPV1-6), which exhibit varying channel properties, tissue expression and physiological functions[2,3]. Primarily expressed in epidermal and hair follicle keratinocytes, the thermo-sensitive, $Ca^{2+}$-permeable, and nonselective TRPV3 channel plays a crucial role in skin physiology including skin barrier formation, hair growth, wound healing, and cutaneous pain and itch sensation[4–9]. Genetic mutations with elevated basal channel activity are associated with abnormal hair morphogenesis, impaired skin barrier, and the human skin disease, Olmsted syndrome[10,11]. Therefore, antagonizing TRPV3 presents a potential therapeutic opportunity for the treatment of skin disease and management of pain and itch.

TRPV3 is activated by warm temperatures as well as numerous chemicals, including plant extracts, lipid metabolites, and synthetic small molecules such as 2-aminoethoxydiphenyl borate (2-APB)[8,12–14]. Unlike many other TRP channels, TRPV3 experiences sensitization, instead of desensitization, upon repeated stimulation by heat or agonists[15–17]. To better understand the unique properties of TRPV3 and to establish a foundation for rational therapies, detailed structural information and mechanistic insight into channel activation through different modalities are required. Toward this end, recent cryo-electron microscopy (cryo-EM) studies have provided a structural description of TRPV3[18–21], exhibiting a similar overall architecture as other thermo-sensitive TRPV channels[22–25]. Each channel subunit, from the amino- to the carboxy- terminus, consists of a cytoplasmic ankyrin repeat domain (ARD), a linker domain, an S1-S4 domain, an S5-S6 pore domain, a TRP domain, and a C-terminal domain. Intriguingly, a collection of distinctive TRPV3 conformations has been observed from different biochemical preparations, in which certain conformations have been assigned as the closed, sensitized and open structures[18–20]. Surprisingly, structures of the mouse and human TRPV3 in the assumed closed state are discernibly different[18,19], and concomitantly different structural mechanisms of gating have been proposed[18,20]. In mouse TRPV3, three putative 2-APB binding sites have been identified, and 2-APB binding to the extracellular portion of the S1-S4 domain has been suggested to play a major role in channel activation by displacing an inhibitory resident lipid, leading to allosteric opening of the ion conduction pore[18]. Notably, application of 2-APB to the wild-type mouse TRPV3 gives rise to a conformation identical to that of the apo state, and the open structure was obtained by applying 2-APB to a mouse TRPV3 variant Y564A[18]. Interestingly, application of 2-APB to

a presumably silent human TRPV3 mutant T96A renders non-conductive conformations distinct from the apo state, including structures with reduced symmetry that deviate from the canonical four-fold symmetric assembly arising from four identical subunits[19]. The putative open structure of human TRPV3 was subsequently achieved by applying 2-APB to a 'sensitized' mutant K169A on the T96A background[20]. In contrast to the mouse TRPV3 study, a single 2-APB binding site, rather than three, was found in human TRPV3[20].

These recent structures illustrate the complex conformational landscape of TRPV3, but with considerable discrepancies as noted above[18–20]. Meanwhile, structures of TRPV1, a close homolog of TRPV3, in distinct functional states elegantly reveal a dual gating mechanism involving pronounced structural rearrangements at both the extracellular selectivity filter (SF) and intracellular S6 helix bundle-crossing (HBC) regions[23], which are in accordance with earlier observations that the selectivity filter region actively contributes to gating elicited by multiple physiological stimuli, including spider toxins, protons, and heat[26–31]. Interestingly, thiol-reactive ions permeate the selectivity filters of TRPV1-3 channels in the presumably closed states in the absence of activating stimuli, suggesting that the structurally dynamic selectivity filters may not serve as activation gates but enable external stimuli to allosterically trigger the opening of the S6 HBC gates[32]. Analogous to TRPV1, in TRPV3, multiple mutations (N643S, I644S, N647Y, L657I and Y661C) specifically diminishing heat activation have been identified at the outer pore region immediately surrounding the selectivity filter[33], and nearby residues I652 and L655 undergo temperature-dependent conformational changes as assessed by cysteine accessibility experiments[34]. These results indicate that the selectivity filter region contributes to channel gating. However, in all reported TRPV3 structures to date, the selectivity filter is adequately wide for ion conduction and appears not to be involved in gating[18–20].

Notably, these previous studies examined TRPV3 in detergents or amphipols[18–20], which are essentially devoid of lipids. The surrounding environments of embedded channels in these reconstitution systems are dramatically different from those of cell membranes composed of phospholipids. Importantly, lipids have been increasingly recognized as indispensable structural and functional components for many integral membrane proteins including TRP channels[35,36]. Consequently structures of integral membrane proteins obtained in detergents or amphipols could very well differ from their more native conformations in a lipid membrane[37–39]. The plasma membrane lipid phosphatidylinositol 4,5-bisphosphate and an endogenous lipid metabolite resolvin D1 have been reported to inhibit TRPV3[40,41]. Farnesyl pyrophosphate, an intermediate in the biosynthesis of steroid hormones, specifically activates TRPV3, but not other related thermo-sensitive TRPV channels[8]. Polyunsaturated fatty acids also potentiate TRPV3[42]. These results underscore the intimate relationship between TRPV3 and lipids, and thus warrant structural analysis of TRPV3 in a lipid membrane environment for better understanding of channel gating in a physiologically relevant setting. Here we present multiple cryo-EM structures of human TRPV3 embedded in lipid nanodiscs, presumably representing conformations in the closed, open and inactivated states at near-atomic resolution. These structures identify critical channel-lipid interactions and reveal a dual gating mechanism, providing unique mechanistic insight into TRPV3 activation and inactivation in a membrane-like environment. Our results

dramatically differ from recent studies using detergents and amphipols[18–20], highlighting the indispensable role of lipids in channel structure and function.

## Results

### Structure of human TRPV3 in lipid nanodiscs

We expressed the wild-type full-length human TRPV3 channel containing residues 1-790 in yeast *Pichia pastoris* and purified the protein to homogeneity. However, the isolated protein in several detergent micelles was prone to aggregation, preventing high-resolution single-particle cryo-EM analysis. In line with this observation, a functionally silent mutation T96A with enhanced biochemical stability, was necessarily introduced to obtain human TRPV3 structures in amphipols[19]. Prompted by the intimate interplay of TRPV3 and lipids and successful application of lipid nanodiscs in cryo-EM studies of membrane proteins including TRP channels[36], we decided to conduct our structural analysis using lipid nanodiscs. We purified the wild-type full-length TRPV3 channel in detergents and then reconstituted the protein into nanodiscs composed of soybean polar lipids and the membrane scaffold protein 2N2 (MSP2N2). Indeed, TRPV3 in nanodiscs migrated as a monodisperse peak in size-exclusion chromatography (Extended Data Fig. 1a, b) and negative-stain electron microscopy further confirmed homogeneous channel-nanodisc particles (Extended Data Fig. 1c).

We determined the cryo-EM structure of human TRPV3 in the absence of ligand in nanodiscs to an overall resolution of 3.1 Å with C4 symmetry imposed (Extended Data Fig. 2 and Table 1). The cryo-EM density map allowed us to build an atomic model including most residues from 117 to 755 (Fig. 1a–e, Extended Data Fig. 2). The N-terminal 116 and C-terminal 35 residues are not resolved in the cryo-EM density and therefore are not modeled. Although the overall structure of the ligand-free human TRPV3 channel in a lipid bilayer is similar to ligand-free structures in detergents and amphipols[18,19], the ion conduction pore structures are markedly different, which will be elaborated later. Like other TRPV channels[22–25,43–45], TRPV3 forms a four-fold symmetric tetramer, with each protomer consisting of an N-terminal ARD, a linker domain, a transmembrane domain (TMD) with six transmembrane helices (S1-S6), a characteristic TRP helix, and a C-terminal domain (CTD) (Fig. 1d,e). In the membrane, the voltage sensor-like S1-S4 domains and the pore domains, comprising S5, the pore helix and S6, are arranged in a domain-swapped fashion, in which the S1-S4 domain from one subunit packs against an adjacent pore domain, mediated by the S4-S5 helical linker (Fig. 1d,e). As in reported TRPV3 structures[18,19], the CTD forms a more extended structure than those observed in other TRPV channels to date, generating an extensive cytoplasmic assembly interface in combination with the ARD from an adjacent subunit (Fig. 1f). This inter-subunit interface defines a common structural motif in TRPV channels that is essential for gating[19,20,22,24].

Well-ordered lipid-like densities with a head-and-two-tails shape, presumably corresponding to tightly associated phospholipids, are located at crevices surrounding the channel (Fig. 1a–e, Extended Data Fig. 3). Similar to TRPV1, TRPV5, and TRPV6 structures in nanodiscs and a voltage-dependent $K^+$ channel crystallized in complex with lipids[36,45–47], multiple annular lipids reside at the inter-subunit interface in the outer leaflet surrounding the pore

domains, potentially reinforcing the domain-swapped configuration in the membrane. The lipid at site 1 simultaneously interacts with the extracellular portion of S4 from one subunit and S5-S6 from a neighboring subunit. The lipid at site 2 is tightly sandwiched between the S5 and pore helices from one subunit and S6 from an adjacent subunit. Site 3 is located in the vicinity of the extracellular portion of S1 facing the pore helix from a neighboring subunit. The head groups of these lipids would be positioned at the boundary of lipid bilayers, most likely interacting with polar residues from the channel, such as Y460, Y461, S626, and Q645 (Extended Data Fig. 3a).

In addition to the annular lipids near the outer pore region, strong lipid-like densities are also present in the inner leaflet. Consistent with recent studies[18,19], non-proteinaceous density is found at site 4 in the pocket created by the intracellular portion of the S1-S4 domain facing the TRP helix (Fig. 1d,e; Extended Data Fig. 3b), a common lipid-binding site for TRPV channels including TRPV1, TRPV2, TRPV5, and TRPV6[24,36,43,45]. Interestingly, the lipid at site 5 is located between the beginning of the helical S4-S5 linker (S571) and the end of a neighboring S4-S5 linker (H585) (Extended Data Fig. 3c). As the S4-S5 linker has been recognized as a critical structural element coupling pore opening and ligand activation in TRP channels as well as voltage activation in voltage-gated ion channels (VGIC)[36,46], this particular lipid is thus conveniently positioned to modulate allosteric coupling.

## Ion conduction pore in lipid bilayer

In the ligand-free structure of TRPV3 in nanodiscs, calculation of the pore radius along the ion permeation pathway indicates two prominent constriction sites, one at the extracellular SF and the other one at the intracellular HBC (Fig. 2a–c). The narrowest point is located at G638 in the selectivity filter, with an interatomic distance of 4.5 Å between diagonally opposed carbonyl oxygen atoms. Interestingly, the bulky hydrophobic side chains of L639 in the selectivity filter ‘$^{638}$GLGD$^{641}$’ point sideways, thus not restricting the dimension of the central ion conduction pore. In contrast, the side chains of the equivalent hydrophobic residue M644 in TRPV1 protrude into the central axis, contributing to the formation of the SF constriction[22,23]. An acidic residue D641 (D646 in TRPV1), important for inhibition by extracellular $Mg^{2+}$ and ruthenium red[48,49], lines the outer pore entrance. The hydrophobic seal at the intracellular HBC gate is constructed by side chains of I674 from S6 helices, with an interatomic diameter of 5.3 Å (diagonal Cα-Cα distance 10.2 Å), which is sufficiently narrow to prevent ion passage.

The ion-conduction pore profile and the dimensions and constituents of both the upper and lower constrictions are strikingly similar to those of TRPV1 in the ligand-free, closed state[22,23,36] (Fig. 2a,c). This remarkable resemblance is in line with the observation that TRPV1 and TRPV3 can form functional heteromeric channels possessing a hybrid pore[50]. Both constrictions undergo substantial widening upon activation in TRPV1[23]. By comparison, it strengthens the conclusion that TRPV3 in a lipid bilayer consists of two physical constrictions along the ion permeation pathway and that the ligand-free structure represents a closed state. Notably, as in TRPV1 and TRPV5[22,23,47], the pore-lining helix S6 in TRPV3, in the closed conformation, contains a π-helical segment beginning at F666 (Fig. 2a), which has been proposed to be involved in TRP channel gating through a local α-to-π

helical transition[18,19,24,45,51] (Fig. 2a,c). In sharp contrast, in TRPV3 structures in the ligand-free, non-conducting state in detergents and amphipols, S6 is entirely α-helical and the selectivity filter is unrestricted for ion conduction (Fig. 2d,e)[18–20].

## Opening in a lipid bilayer

The cryo-EM structure indicates that the ligand-free wild-type TRPV3 channel in a lipid bilayer favors a closed conformation. Of the known chemical ligands, 2-APB is the most potent and commonly used TRPV3 agonist[12], but promiscuously activates or inhibits other TRP channels, including TRPV1, TRPV2, TRPV6, TRPA1, TRPM2, TRPM6, TRPM7, TRPC3, TRPC6, and TRPC7[12,52–56]. Repeated application of 2-APB sensitizes TRPV3 (Fig. 3a)[15,57], but at high concentrations 2-APB and its analogues reportedly inhibit the channel[48]. These observations indicate an intricate mode of action by 2-APB, which potentially presents a challenge to achieve an open conformation of TRPV3 bound with 2-APB. Consistently, recent studies reported that application of 2-APB to wild-type channels did not yield an open conformation[18,19]. Repetitive application of 2-APB to human TRPV3 resulted in a ‘sensitized’ conformation in amphipols[19], which is similar to our apo, closed wild-type structure in nanodiscs, except for a wider selectivity filter.

Neutralization of a basic residue K169 from the ARD, which forms important salt-bridge interactions with acidic residues E751 and D752 from the distal CTD of an adjacent subunit at the cytoplasmic inter-subunit interface (Fig. 1f), sensitizes the channel and facilitates opening[17,20]. In excised inside-out membrane patches, the wild-type TRPV3 channels show pronounced use-dependent increase in current response elicited by repeated application of 30 μM 2-APB and reach the maximal current following ~30 cycles of stimulation (Fig. 3a–c). The first application typically only induces ~17% of the maximal current response. In contrast, the charge-neutralization mutant K169A readily approaches the maximal response in the first two or three rounds of stimulation and the initial response reaches 90% of the maximum. Additionally, a much larger fraction of current response remains following removal of 2-APB in membrane patches containing K169A channels, compared with patches with wild-type channels. These results indicate that K169A not only sensitizes the channel but also stabilizes the open conformation. In excised membrane patches without application of 2-APB, K169A shows robust spontaneous opening leading to increased current amplitude in minutes, indicating a higher basal open probability than the wild type (Fig. 3d,e). The relative basal open probability of K169A, indicated by the current ratio in the absence to presence of 2-APB, is 0.57 ± 0.08 (Fig. 3e).

Motivated by these results, we determined the cryo-EM structure of the human TRPV3 K169A variant embedded in nanodiscs to gain insights into channel gating in a lipid bilayer (Fig. 3f and Extended Data Fig. 4). 3D classification identified two major conformations, which presumably represent the open (~69%) and inactivated states (~31%) that we will discuss in detail (Extended Data Fig. 4). Consistent with its increased basal activity, K169A in the absence of ligand indeed produced an open conformation, as assessed by interatomic distances and pore radius calculation (Fig. 3g,h). Both the SF and HBC constrictions are considerably expanded. The pore-lining helix S6 maintains its secondary structure, containing a π-helical turn in the middle, as in the closed conformation and the same set of

amino acids define the narrowest points along the ion pore. The interatomic distances between the diagonal backbone carbonyl oxygen atoms of G638 and between the diagonal carbon atoms of the side chains of I674 increase from 4.5 to 6.9 Å, and from 5.3 to 9.2 Å (diagonal Cα-Cα distance 13.2 Å), respectively. This open pore conformation is similar to those determined in detergents and amphipols[18,20], and the degree of opening is analogous to that of TRPV1[23]. Overall, the open structure of ligand-free K169A in lipid nanodiscs resembles the open structures of the mouse TRPV3 Y564A variant in detergents and the human TRPV3 K169A mutant in amphipols bound to 2-APB[18,20]. Surprisingly, in human TRPV3, K169A in the absence of 2-APB gives rise to an open conformation in lipid nanodiscs but a non-conducting conformation in amphipols[20], underscoring the importance of lipid modulation of channel activity.

To better understand TRPV3 gating transitions in a lipid bilayer, we aligned the open K169A with closed wild-type structures and observed global conformational changes in both the transmembrane and cytoplasmic domains upon channel opening (root mean square deviation (r.m.s.d) of all Cα ~2.8 Å, Fig. 4a,b). The nature and extent of domain movements are comparable to those in TRPV1 activation[23] (Extended Data Fig. 5). Disruption of salt bridge interactions through the K169A mutation results in a drastic secondary structure change at the distal CTD (Fig. 4c,d), which transitions from an extended loop to an α-helix. This structural rearrangement is in agreement with previous human TRPV3 studies in amphipols, in which the loop-to-helix transition was proposed to function as a conformational switch for TRPV3 activation that is likely applicable to other TRPV channels[20]. In our open TRPV3 structure, it appears that the distal C-terminal helix pushes the Finger 5 loop of an adjacent ARD counterclockwise, viewed from the intracellular side (Fig. 4c,d), and this structural rearrangement would propagate to the linker domain, the TRP helix, and the transmembrane domain, eventually resulting in central pore opening.

Upon channel opening, each of the four pore-lining S6 helices moves outward by ~1.3 Å with a marginal rotation of ~3°. Consequently, the subtle yet collective outward movement of the pore-lining helices results in an expansion of the HBC gate (Fig. 4e). The selectivity filter dilates as the SF loops move away from each other, accompanied by repositioning of the pore helix with a downward movement of ~2 Å and a rotation of ~8° (Fig. 4e,f). In the closed conformation, one of the acyl chains of an ordered lipid at site 2 snugly fits in the hydrophobic crevice between the pore helix and S6 π-helical segment and appears to physically support the up configuration of the pore helix (Fig. 4f). The downward movement of the pore helix associated with channel gating would require the lipid tail withdrawn from this pocket, which is precisely illuminated in the open structure (Fig. 4g). In addition, the lipid head group shifts downward together with the pore helix, as indicated by the head-and-two-tails shape of lipid density (Fig. 4g).

Lipid rearrangement during channel activation also occurs in the ligand or lipid binding pocket shared by TRPV channels, which is located in the vicinity of the S4-S5 linker and TRP helix facing the interface between the S1-S4 and pore domains[24,36,43,45] (Extended Data Fig. 6). First described in TRPV1, this binding site accommodates a resident lipid, vanilloid ligands, or antagonists to differentially modulate channel activity[36]. The lipid density, albeit weaker, appears in the corresponding locale in TRPV3 embedded in

nanodiscs in the closed conformation but becomes more prominent in the open conformation (Extended Data Fig. 6). This observation further supports the important role of this conserved ligand binding site in shaping channel activity, and mutagenesis of key residues involved in this site has rendered TRPV2 and TRPV3 channels sensitive to TRPV1-specific vanilloid agonist resiniferatoxin (RTX)[58–60]. Lipid rearrangement also occurs at site 5 between inter-subunit S4-S5 linkers, and the lipid bound in the closed conformation essentially dissociates from the channel upon activation.

## Channel inactivation

In excised membrane patches, both the wild-type and K169A channels gradually inactivate with sustained stimulation by 2-APB (Fig. 5a–c). Therefore, we conducted cryo-EM studies of the wild type and K169A in the presence of 2-APB throughout the purification and reconstitution procedures to attain structural insights into channel inactivation. We obtained a 3D reconstruction at low resolution for the wild type but determined the structure of K169A with 2-APB bound at a medium resolution of 4.3 Å, which was used in our structural analysis (Fig. 5d, Extended Data Fig. 7). The cryo-EM density is of sufficient quality at a moderate resolution, and the majority of side chain densities is well resolved (Extended Data Fig. 7f), thus facilitating model building at high confidence (Fig. 5d). Likely owing to the limited resolution, the cryo-EM density does not show well-ordered lipid molecules surrounding the channel, as observed in the closed and open structures. The overall structure is similar to the ligand-free, open structure of K169A (r.m.s.d of all $C_\alpha$ atoms ~1.7 Å), except for pronounced structural rearrangements centered at the pore-lining helix S6 (Fig. 5e–g). The pore structure in the inactivated state closely resembles those in the assumed closed states of TRPV3 in detergents and amphipols[18,19]. In the inactivated conformation, while the selectivity filter is comparable to that in the open structure, S6 becomes entirely α-helical, generating dramatic rearrangements of the intracellular half of S6 beginning at F666, where the π-helical segment begins in the closed and open structures. The S6 π-to-α transition results in an inward contraction of ~10° toward the central axis for the lower half of S6, accompanied by a rotation of ~100° about the axis of the helix (Fig. 5f). Subsequently a different set of amino acids of the lower half of S6 faces the ion conduction path on the intracellular side, and M677, instead of I674, lines the intracellular S6 HBC gate in the inactivated conformation. The C-terminal end of S6 partially unwinds, creating a more relaxed connector joining S6 and the TRP helix (Fig. 5g). Thus, it appears that upon inactivation the pore domain is less tightly coupled to the TRP domain.

Robust non-protein density in the vicinity of H426, which has been independently identified as a binding site that is specifically important for 2-APB sensitivity[18,20], indicates that 2-APB is bound in our inactivated structure (Fig. 6a). In contrast, the same binding pocket is clearly unoccupied in the ligand-free wild type and K169A structures (Fig. 6b,c). To verify that the inactive K169A structure in the presence of 2-APB stems from continued exposure of the channel to 2-APB, we also determined the cryo-EM structure of K169A briefly introduced to 2-APB for 3 minutes (Extended Data Fig. 8), which is essentially identical to the ligand-free, open K169A structure (r.m.s.d of all Cα ~0.7 Å), except for prominent non-protein density attributable to 2-APB appearing in the ligand-binding pocket (Fig. 6d). This result further confirms that 2-APB is readily accommodated by the open conformation. We

did not observe additional densities likely representing 2-APB molecules in the 2-APB-bound open and inactivated structures. Thus, the fact that K169A channels spontaneously open in the absence of 2-APB and 2-APB binds to both the open and inactivated structures makes it premature to explain the complex mode of action by 2-APB.

In the previous mouse TRPV3 study, two additional 2-APB binding sites have been proposed, including site 4 in the intracellular portion of the S1-S4 domain that binds lipid (Extended Data Fig. 3b)[18]. The introduction of a point mutation Y564A at this site in mouse TRPV3 gives rise to an increase of apparent 2-APB affinity[18], supporting its role in 2-APB binding. However, the non-proteinaceous density at site 4 is present in all of our TRPV3 structures in nanodiscs, in the absence and presence of 2-APB. This result is also consistent with the observation of non-protein density at site 4 in human TRPV3 structures in amphipols, with and without application of 2-APB[19]. Additionally, the H426A mutation in the consensus 2-APB binding site results in reduced response to high concentrations of 2-APB but maintains sensitivity to camphor[20]. In contrast, mutations at site 4 in human TRPV3 do not alter relative responses of 2-APB compared to camphor[20]. These results indicate that site 4 is not involved in 2-APB-dependent activation in human TRPV3. On the other hand, crystallographic studies using brominated derivative of 2-APB identified that 2-APB binds to the equivalent location of site 4 in TRPV6 to inhibit the channel[56]. Collectively, these results suggest that the location at site 4 could be a lipid or ligand binding site common to TRPV channels that can differentially modulate channel activity.

## Discussion

In this work, multiple cryo-EM structures of human TRPV3 embedded in lipid nanodiscs, representing distinct functional states, have illuminated gating transitions in a lipid bilayer environment, which are remarkably different from those observed in detergents and amphipols[18–21]. The ligand-free, closed conformation of TRPV3 in nanodiscs reveals a unique non-conducting conformation with two physical constrictions along the ion permeation pathway, which has evaded previous studies in detergents and amphipols[18–21]. Both the upper SF and lower S6 HBC regions are narrow in the closed state and expand considerably upon channel activation, accompanied by pronounced lipid rearrangements surrounding the channel. The pore-lining helix S6 maintains a π-helical turn transitioning from the closed to open conformation, but becomes entirely α-helical in the inactivated state (Extended Data Fig. 9). Our structures, in combination with functional characterization, provide visualization of human TRPV3 activation and inactivation in a lipid bilayer that closely resembles biological membranes. In line with recent structural studies of TRPV3[18–21], it has proven to be a challenge to obtain open structures of the wild-type channel. Here in this work, we leveraged the K169A sensitization mutant to obtain the open and inactivated structures at near atomic resolution to gain insight into channel gating in a lipid bilayer, which might differ from gating of the native TRPV3 channels by physiological stimuli.

Multiple lipid molecules position in the vicinity of critical structural elements of human TRPV3 in nanodiscs and rearrange during gating. In the previous study of mouse TRPV3 in detergents, lipid density was reported at a location between the extracellular half of S4 and

the pore domain in the ligand-free state, and it was proposed that 2-APB binding to a nearby site created by the extracellular portion of the S1-S4 domain allosterically displaces this inhibitory lipid, resulting in tighter association of the S1-S4 and pore domains, promoting channel opening[18]. In contrast, in our human TRPV3 structure in nanodiscs as well as in human TRPV3 structure in amphipols[19], S4 packs tightly against the pore domain and the corresponding lipid is not present. It remains unclear what gives rise to this discernible structural difference and hence potential gating transitions, which may reflect amino acid sequence divergence between the human and mouse orthologs.

The narrow SF in the closed conformation of TRPV3 in a lipid bilayer is also in drastic contrast to the wide selectivity filters observed in all structures determined in detergents and amphipols, which led to the suggestion that the selectivity filter is not involved in TRPV3 gating[18–21]. This notion directly contradicts our structures in lipid nanodiscs as well as previous functional data supporting the involvement of the SF in channel activation. Multiple residues (N643S, I644S, N647Y, L657I and Y661C) surrounding the selectivity filter and pore helix have been identified as critical for heat activation[33], and immediately nearby residues (I652 and L655) exhibit temperature-dependent cysteine accessibility[34]. In a more recent study, sensitivity of the TRPV1-specific ligand RTX was introduced to TRPV3 by point mutations creating a vanilloid-binding pocket (the TRPV3-6M construct)[60]. However, activation of the engineered TRPV3-6M by RTX requires additional point mutations in the outer pore, elevated temperature, or sensitization by 2-APB[60], suggesting physically separated activation pathways. In TRPV1, agonist binding specifically stabilizes opening of the S6 HBC gate, leaving the SF constriction virtually unaltered. In analogy, RTX binding in the engineered TRPV3 channel may facilitate opening of the HBC gate but stimulation by heat or 2-APB would be additionally required to support the expanded SF configuration to stabilize the open pore. The five individual pore mutants, V587L, A606V, F625L, F656I, and F666Y, enabling channel activation by RTX cluster at the surrounding of site 1 lipid (Extended Data Fig. 10), which facilitates the maintenance of a narrow selectivity filter. This observation further supports the critical role of lipid 1 in channel gating. Additionally similar to TRPV1, the TRPV3-6M channel exhibits allosteric coupling between heat and vanilloid activation[60].

These results also raise an interesting possibility regarding the mechanism of temperature sensation in TRPV3. Comparison of the narrow SF in nanodiscs and the wide SF in detergents or amphipols in the absence of ligand suggests that resident lipids may facilitate closure of the SF and elevated temperature would rearrange these lipids to expand the SF. This concept was introduced earlier in TRPV1 on the basis of structures determined in nanodiscs[36]. An endogenous lipid, putatively assigned as phosphatidylinositol, was found at the agonist-binding pocket in the ligand-free, closed TRPV1 channel, and it appears that agonist binding or elevated temperature would expel this resident lipid to activate the channel. TRPV1 and TRPV3 may share basic principles in ligand and temperature activation, given the remarkable similarity of the closed and open conformations, as well as allosteric coupling between distinct activation pathways in TRPV1 and TRPV3 channels.

# Methods

## Protein expression and purification

The full-length human TRPV3 DNA (GenBank: EAW90503.1) was cloned into a modified pPICZ-B vector with a PreScission protease cleavage site and a C-terminal GFP-$His_{10}$ tag for protein expression. The human TRPV3 K169A mutant was generated by site directed mutagenesis. For electrophysiological recordings, DNA fragments corresponding to the wild type or mutant TRPV3 channels were ligated into a modified pCEU vector with a C-terminal GFP-$His_8$ tag.

The wild-type and mutant human TRPV3 channels were expressed in *Pichia pastoris*. For wild-type protein purification, yeast cells (20 g) were disrupted by milling (Retsch MM400) and resuspended in lysis buffer containing 50 mM Tris-HCl pH 8.0 and 150 mM NaCl supplemented with protease inhibitors (2.5 μg $ml^{-1}$ Leupeptin, 1 μg $ml^{-1}$ Pepstatin A, 100 μg $ml^{-1}$ 4-(2-Aminoethyl) benzenesulfonyl fluoride hydrochloride, 3 μg $ml^{-1}$ Aprotinin, 1 mM Benzamidine and 200 μM phenylmethane sulphonylfluoride) and DNase I. Cell membranes were solubilized for 2 h in buffer containing 2% (wt/vol) n-dodecyl-β-D-maltopyranoside (DDM, Anatrace) with stirring at 4°C and then centrifuged for 0.5 h at 30,000g. Supernatant was added to 3 ml cobalt-charged resin (G-Biosciences), and rotated for 3 h at 4°C. Resin was then washed with 30 ml buffer containing 20 mM Tris-HCl pH 8.0, 150 mM NaCl, 10 mM imidazole, and 4 mM DDM. Protein was eluted with buffer containing 20 mM Tris-HCl pH 8.0, 150 mM NaCl, 200 mM imidazole, and 1 mM DDM. For purification of K169A, cell lysate was extracted with 1% Lauryl Maltose Neopentyl Glycol (LMNG, Anatrace), and the detergent was exchanged to 85 μM glyco-diosgenin (GDN, Anatrace) in the wash and elution buffer.

## Nanodisc reconstitution

Soybean polar lipid extract (Avanti Polar Lipids) in chloroform was dried under argon and then by vacuum desiccation for more than 2 h. Lipids were rehydrated at 10 mM in buffer containing 20 mM Tris-HCl pH 8.0, 150 mM NaCl, and 14 mM DDM, and sonicated right before use. Channel protein eluted from cobalt-charged resin was concentrated to ~ 20 μM and then mixed with the scaffold protein MSP2N2 and lipids and at molar ratio of 1:0.5:50. The mixture was incubated on ice for 10-30 min before the addition of Bio-beads SM-2 resin (Bio-Rad) at a final volume of ~12.5% (vol/vol). PreScission protease was then added to the mixture to remove the C-terminal GFP-$His_{10}$ tag. The mixture was incubated at 4°C overnight with constant rotation. Bio-beads were then removed by centrifugation and the clear reconstitution solution was concentrated and further purified on a Superose 6 column (GE Healthcare Life Sciences) in buffer containing 20 mM Tris-HCl pH 8.0 and 150 mM NaCl.

## Cryo-EM sample preparation and imaging

3.5 μl of purified channel concentrated to ~1 mg $ml^{-1}$ was pipetted onto glow-discharged Quantifoil R1.2/1.3 or R2/2 copper grids (Quantifoil). For sample preparation of K169A briefly exposed to 2-APB, the protein was incubated with 1 mM 2-APB for 3 min before applied to grids. Grids were blotted for 2 s at ~100% humidity and flash frozen in liquid

ethane using FEI Vitrobot Mark IV (Thermo Fisher Scientific). Grids were then transferred to a FEI Titan Krios (Thermo Fisher Scientific) electron microscope operating at 300 kV. Cryo-EM datasets were collected in an automated fashion on a Gatan K2 Summit (Gatan) detector in super-resolution counting mode with a super-resolution pixel size of 0.55 Å (physical pixel size of 1.1 Å) using EPU (https://www.fei.com/software/epu-automated-single-particles-software-for-life-sciences/). GIF Quantum energy filter with a slit width of 20 eV was operated in zero-energy-loss mode before detector. Dose-fractionated images were recorded with a nominal defocus value ranging from −1.0 μm to −2.5 μm. Each movie was recorded for 8 s using a per-frame exposure time of 200 ms and a dose of ~7.8 electrons per $Å^2$ per second, resulting in an accumulated dose of ~62 electrons per $Å^2$.

## Image processing and map calculation

Recorded movies were subjected to motion correction and dose-weighting with MotionCor2[61]. Motion corrected images with dose weighting were used for contrast transfer function (CTF) determination using GCTF[62]. After motion correction and CTF estimation, low-quality images were manually removed from the datasets. For the apo wild-type dataset, ~6,000 particles were manually selected to generate two-dimensional class templates for automated particle picking in RELION2[63]. Particles were extracted using a particle box size of 256 pixels and subjected to 2D classification with a mask diameter of 190 Å. Particles in good 2D classes were selected and imported into cryoSPARC to generate an *ab initio* low resolution map[64]. 3D refinement and 3D classification were performed in RELION2 to select good particles for final 3D refinement and post-processing[63]. For reconstructions of other datasets, the apo wild-type map was low-pass filtered to 60 Å and served as a reference map for 3D classification in RELION3[65]. CTF refinement and Bayesian polishing were performed to improve the map quality, and local resolution estimates were calculated in RELION3[65].

All four datasets were collected from the same Titan Krios microscope using the same imaging conditions. 3D reconstruction for the 2-APB-bound inactivated state has the lowest resolution and local resolution at the 2-APB binding site was estimated to be 4.0 Å. Therefore, to allow direct comparison of the 2-APB binding site, we adjusted the power spectrum of the other three maps to match that of the map of the 2-APB-bound inactivated state using --adjust_power within relion_image_handler, and then low pass filtered all four maps to 4.0 Å using --lowpass within relion_image_handler. These normalized maps were used to identify the 2-APB binding site and to facilitate assignment of the functional states of these distinct conformations. 3D classification of the apo K169A dataset identified two major conformations, which presumably represent the open (~69%) and inactivated states (~31%). The inactivated structure is essentially identical to the K169A-2-APB inactivated structure, except for the absence of 2-APB.

## Model building and refinement

To build the apo wild-type human TRPV3 model, the crystal structure of the isolated mouse TRPV3 ankyrin repeat domain (PDB: 4N5Q) was docked into the cryo-EM density map using UCSF CHIMERA[66], and then manually adjusted in COOT[67]. The remaining structure was *de novo* built into the density map guided by TRPV1 structure and bulky side chains to

register the amino acid sequence. Real space refinement was performed using real_space_refine in PHENIX[68]. The other structures were built by docking the apo wild-type model into cryo-EM density maps in CHIMERA, adjusted in COOT, and further refined in PHENIX. Model validation was performed with MolProbity[69]. Well-resolved lipid-like densities with a head-and-two-tails shape were putatively modeled as phospholipids. For simplicity, all lipids in the structures were modeled as phosphatidylethanolamines (PE), which were generated using eLBOW in PHENIX.

## Electrophysiological recordings

CosM6 cells were transfected with 1-2 μg of plasmids encoding human TRPV3 or K169A with C-terminal GFP using FuGENE 6 (Promega). The cells were used for patching 24-48 h after transfection. Protein expression was assessed by GFP fluorescence. Inside-out membrane patches were excised from the cellular plasma membranes using glass pipettes (Kimble Chase 2502) with BN (bubble number) ~5[70], fabricated with a Sutter P-96 puller (Sutter Instruments). Symmetric potassium internal buffer (140 mM KCl, 4 mM $K_2HPO4$, 1 mM EGTA, 1 mM $K_2EDTA$, pH 7.38) was used in all experiments. Membrane potential was maintained at −20 mV or as specified in the text. The agonist (2-APB) at indicated concentrations was applied to the membrane patches from the cytoplasmic side via continuous bath perfusion. The data were acquired with Axopatch-1D patch-clamp amplifier and Digidata 1320 digitizer (Axon Instruments) at 500 Hz and low-pass filtered at 200 Hz. Data analysis was performed in pClamp 10.6 software suite (Molecular Devices).

For sensitization experiments, protocols consisting of repeated 15 s application of 30 μM 2-APB followed by 45 s washout in the agonist-free buffer were used. The measurements continued for about 30 cycles or until current saturation. The ratio of the 2-APB-induced current in the first cycle and the maximum achievable current was used to estimate sensitization efficiency for the wild type and K169A. In the inactivation experiments, the agonist (1 mM 2-APB) was continuously applied to the patch during the entire course of experiments.

## Cell lines

*Pichia pastoris* SMD1163H (Invitrogen) and CosM6 (monkey kidney fibroblasts) cells were used. Cell lines were not authenticated or tested for mycoplasma contamination.

## Reporting summary

Further information on experimental design is available in the Nature Research Reporting Summary linked to this article.

## Data availability

The cryo-EM maps of the wild-type human TRPV3 and K169A have been deposited to Electron Microscopy Data Bank with accession codes EMD-20917 (apo TRPV3), EMD-20918 (apo K169A), EMD-20919 (K169A with 3 min exposure to 2-APB), and EMD-20920 (K169A in the presence of 2-APB). Atomic coordinates have been deposited to the Protein Data Bank (PDB) with accession codes 6UW4 (apo TRPV3), 6UW6 (apo

K169A), 6UW8 (K169A with 3 min exposure to 2-APB), and 6UW9 (K169A in the presence of 2-APB).

## Extended Data

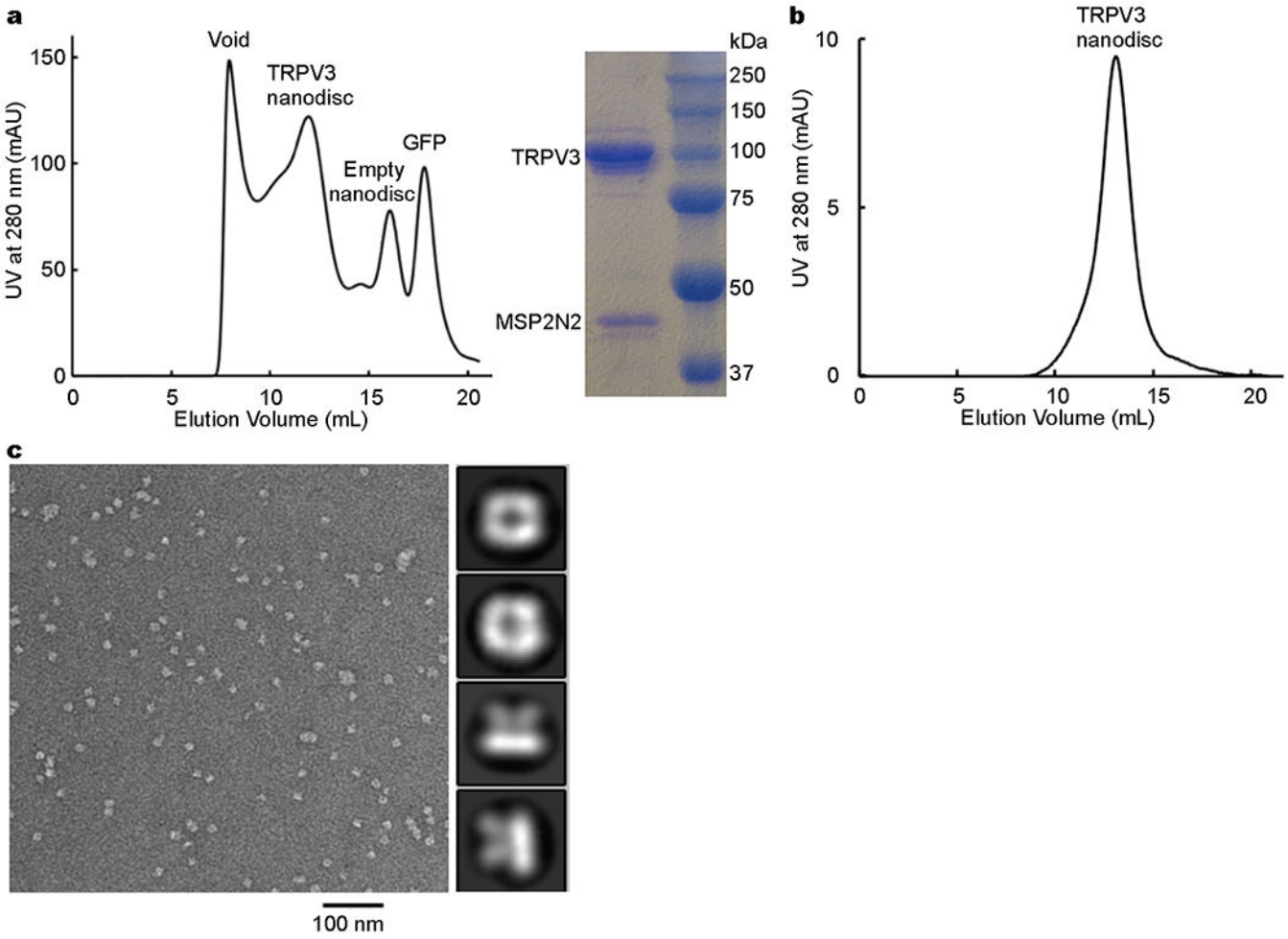


**Extended Data Fig. 1: Reconstitution of human TRPV3 into lipid nanodiscs.**

**a**, Size-exclusion chromatography of TRPV3 reconstituted into lipid nanodiscs made of soybean polar lipids and the scaffold protein MSP2N2 (left panel). Peaks indicating the void, the TRPV3-embedded nanodiscs, the empty nanodiscs, and GFP were labeled. The peak fraction corresponding to TRPV3 channels in nanodiscs was shown on SDS-PAGE (right panel). **b**, The collected TRPV3-nanodisc fraction ran as a monodisperse peak on size-exclusion chromatography. **c**, Representative micrograph for negative stain and reference-free 2D class averages indicating a tetrameric channel inserted into nanodiscs (right).

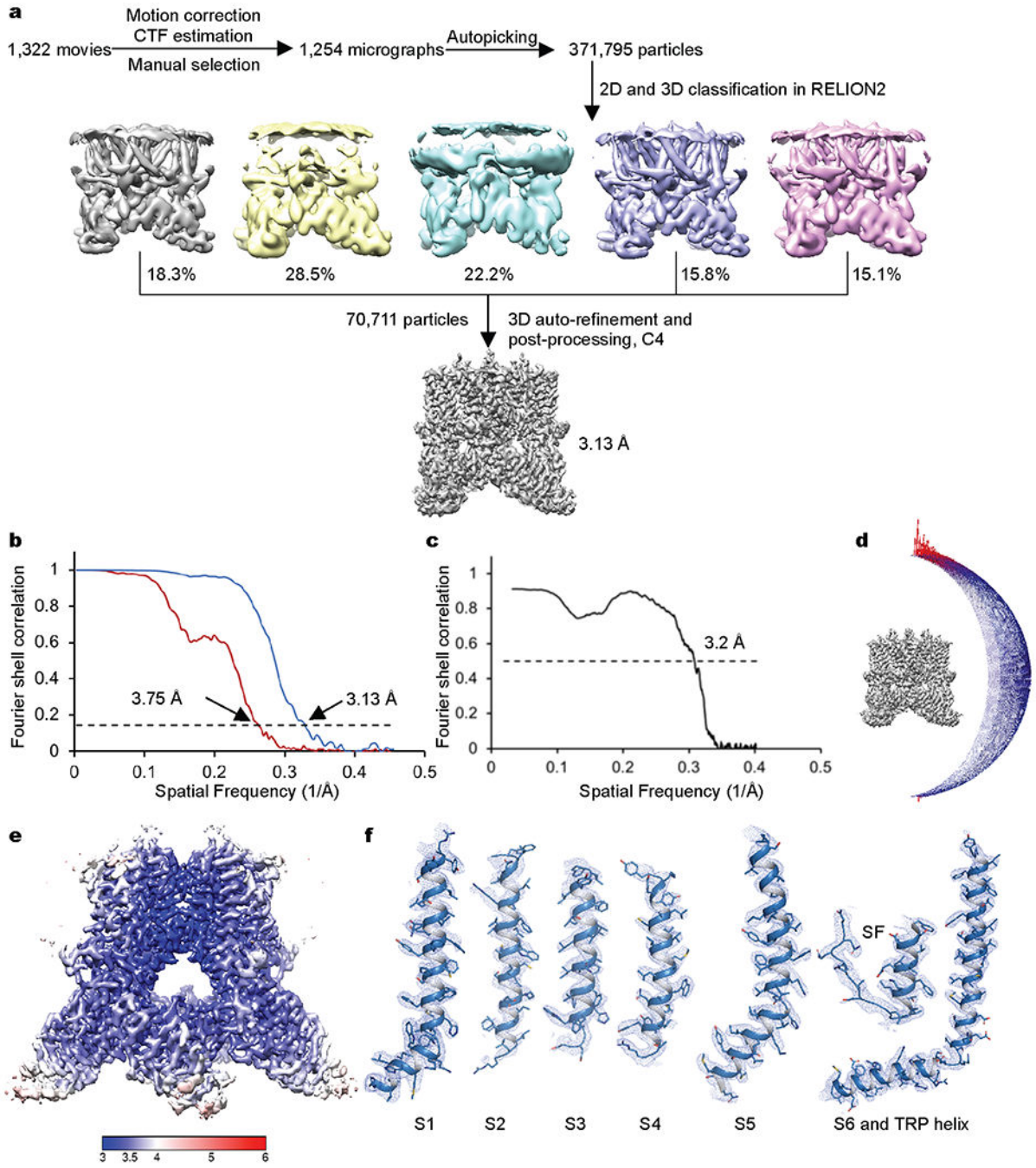


**Extended Data Fig. 2: Cryo-EM reconstruction of the wild-type full-length human TRPV3 in lipid nanodiscs.**

**a**, Flowchart of cryo-EM data processing. **b**, Fourier shell correlation before and after post-processing in RELION2. **c**, Fourier shell correlation between the refined model and the full map. **d**, Angular distribution plot of particles used for final reconstruction. **e**, Cryo-EM density map colored by local resolution. **f**, Representative cryo-EM density shown as blue mesh contoured at 5.0 σ.

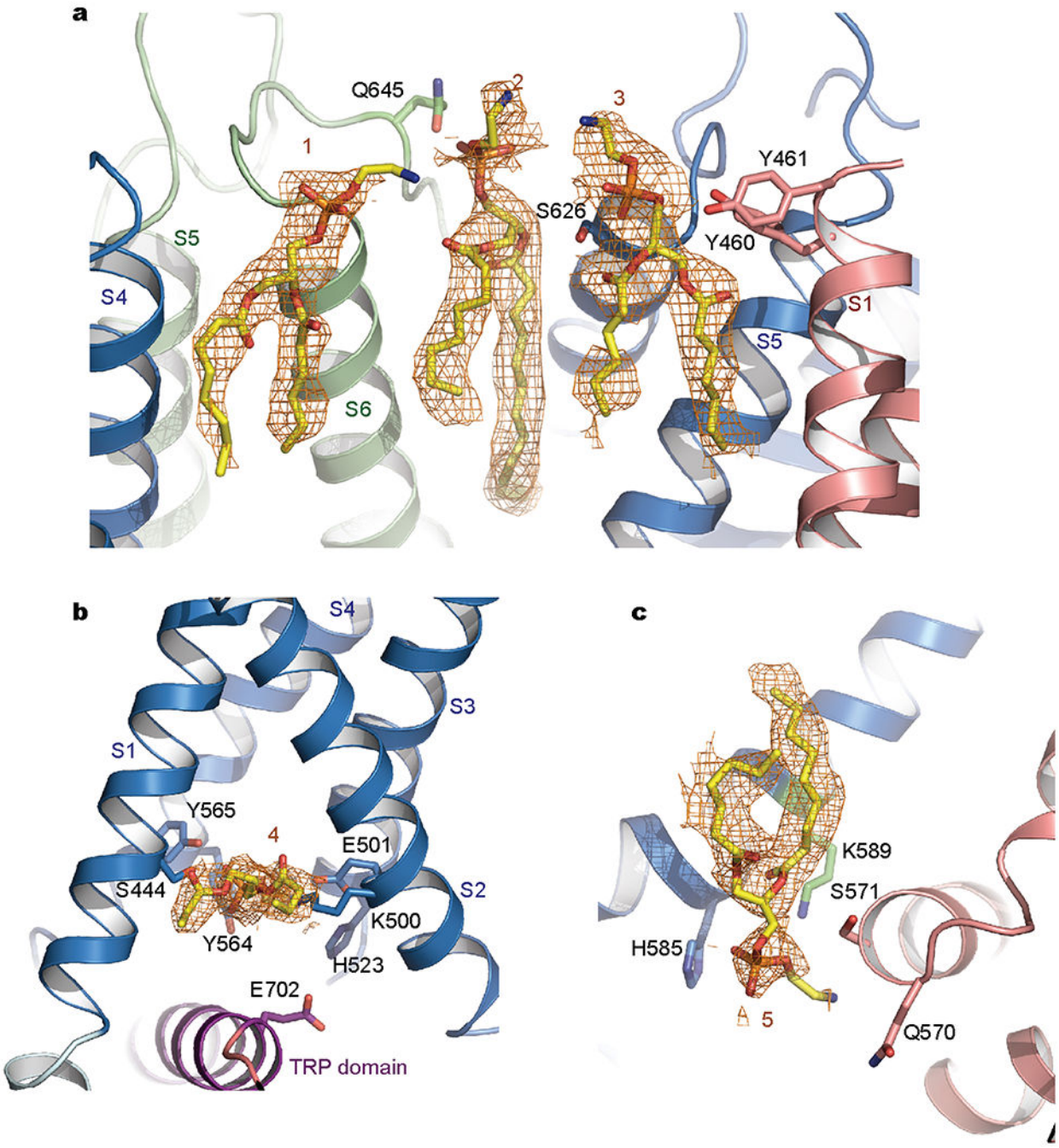


**Extended Data Fig. 3: Channel-lipid interactions in human TRPV3.**

**a**, Lipid densities at sites 1, 2, and 3 located in the proximity of the outer pore region. Lipids are putatively modeled as phosphatidylethanolamine to illustrate interactions with the channel. Channel subunits are uniquely colored. Polar and charged residues potentially interacting with lipid head groups are highlighted in stick representation. **b**, Lipid density at site 4 in the intracellular cavity of the S1-S4 domain. **c**, Lipid density between the S4-S5 linkers of two neighboring subunits. The putative lipid densities are shown as orange mesh contoured at 3.5 σ.

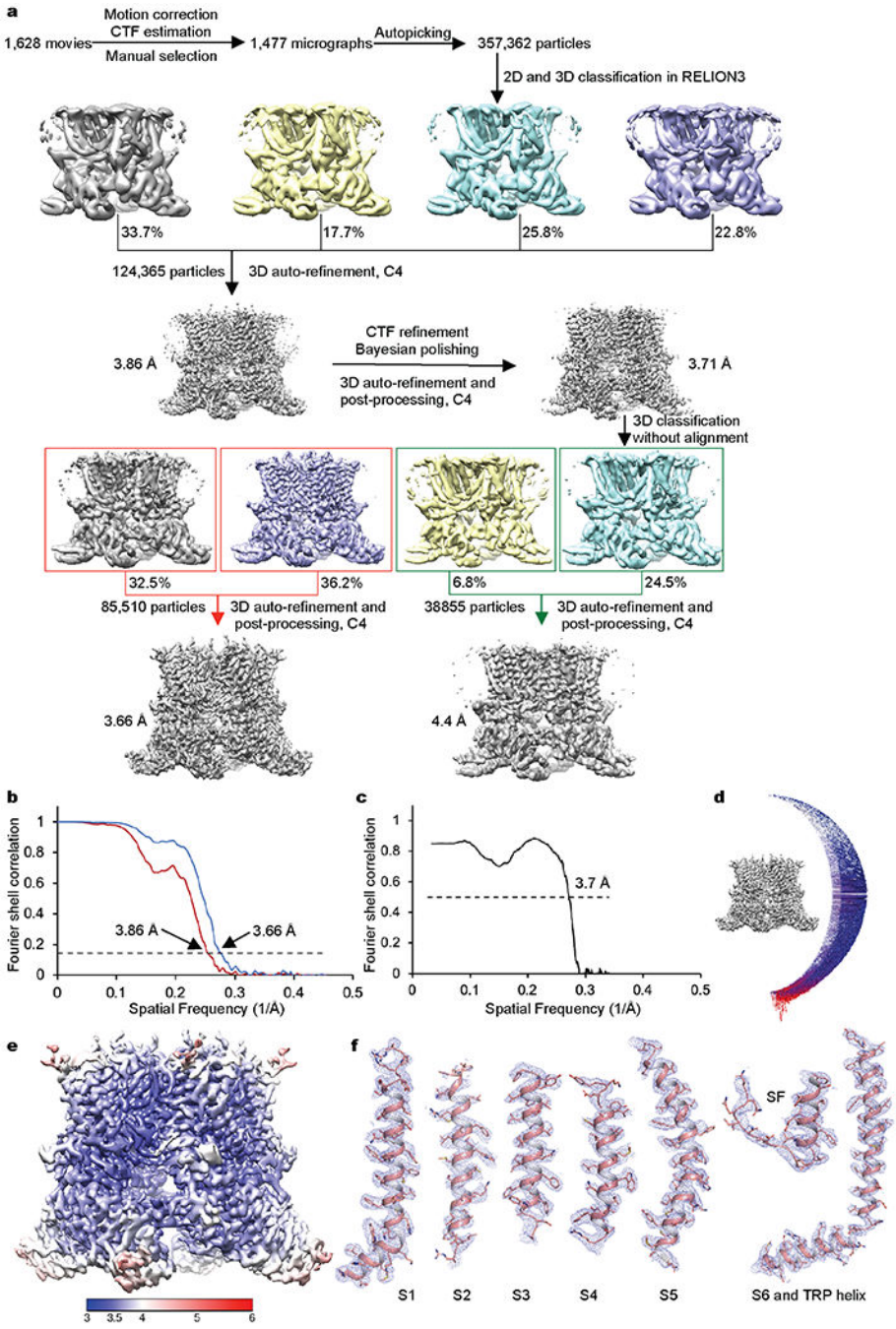


**Extended Data Fig. 4: Cryo-EM reconstruction of the human TRPV3 K169A variant in lipid nanodiscs.**

**a**, Flowchart of cryo-EM data processing. Two major conformations, presumably representing the open (~69%) and inactivated states (31%), were refined to resolutions of 3.66 Å and 4.4 Å, respectively. **b**, Fourier shell correlation before and after post-processing in RELION3 for the open state. **c**, Fourier shell correlation between the refined model and the full map for the open state. **d**, Angular distribution plot of particles used for final

reconstruction for the open state. **e**, Cryo-EM density map colored by local resolution for the open state. **f**, Representative cryo-EM density shown as blue mesh contoured at 5.0 **σ**.

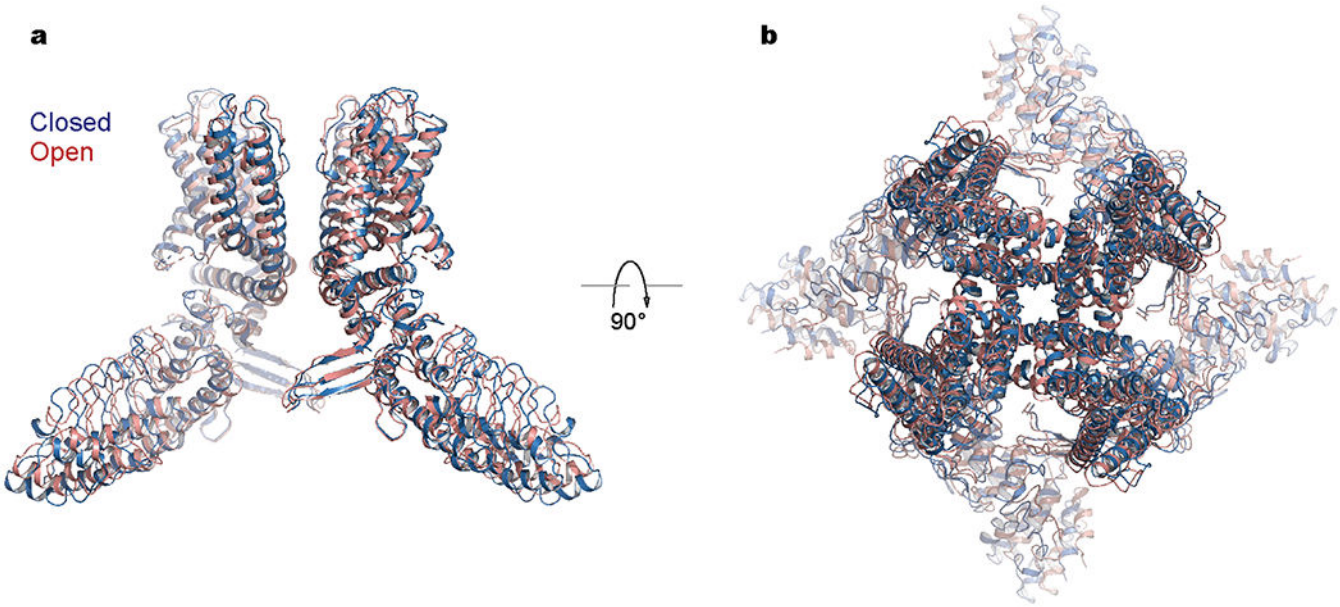


**Extended Data Fig. 5: Opening of TRPV1.**

**a**,**b**, Orthogonal views of the closed (PDB: 3J5P) and open (PDB: 3J5Q) structures of TRPV1.

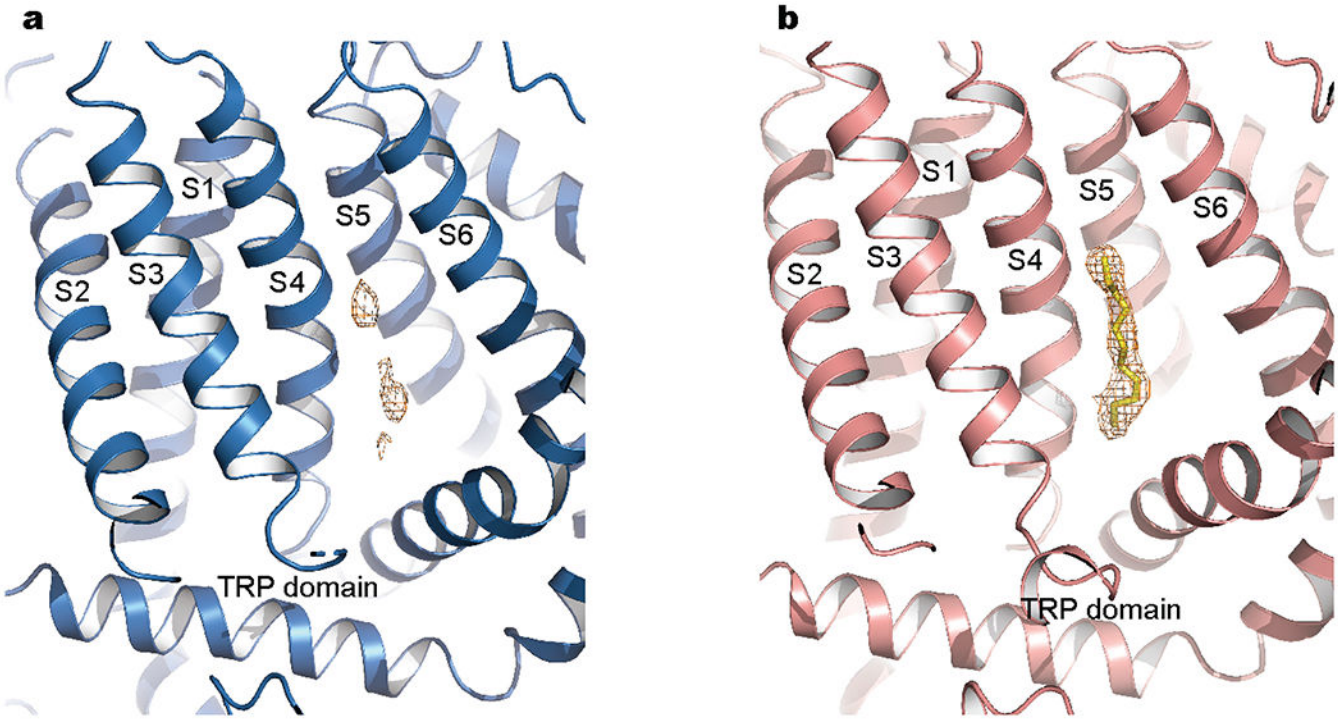


**Extended Data Fig. 6: Lipid in the analogous vanilloid binding pocket in TRPV3.**

**a**,**b**, Putative lipid density shown as orange mesh contoured at 4.5 σ in the analogous vanilloid binding pocket in the closed (**a**) and open (**b**) conformations.

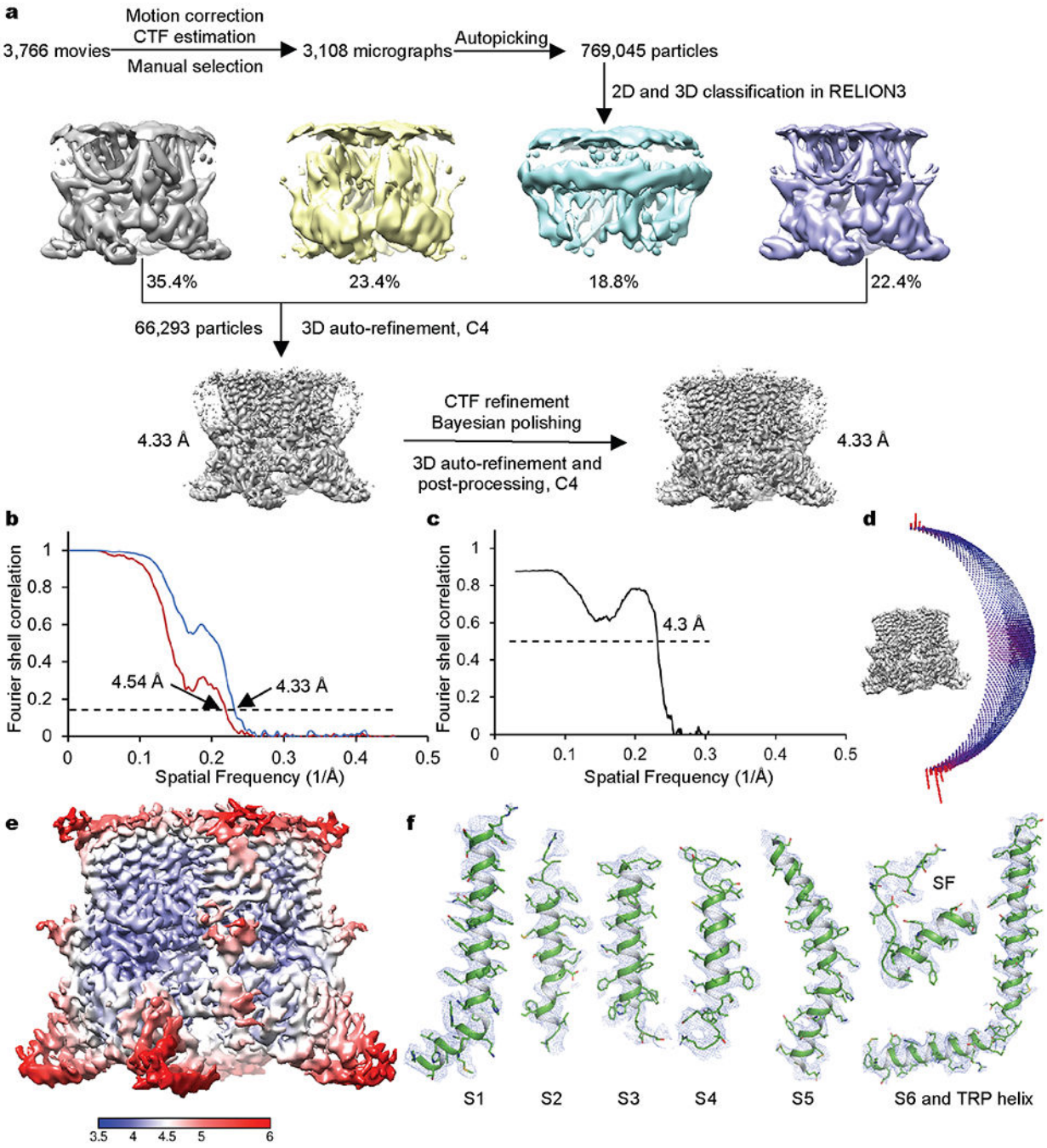


**Extended Data Fig. 7: Cryo-EM reconstruction of K169A accompanied by 2-APB in an inactivated state.**

**a**, Flowchart of cryo-EM data processing. **b**, Fourier shell correlation before and after post-processing in RELION3. **c**, Fourier shell correlation between the refined model and the full map. **d**, Angular distribution plot of particles used for final reconstruction. **e**, Cryo-EM density map colored by local resolution. **f**, Representative cryo-EM density shown as blue mesh contoured at 5.0 σ.

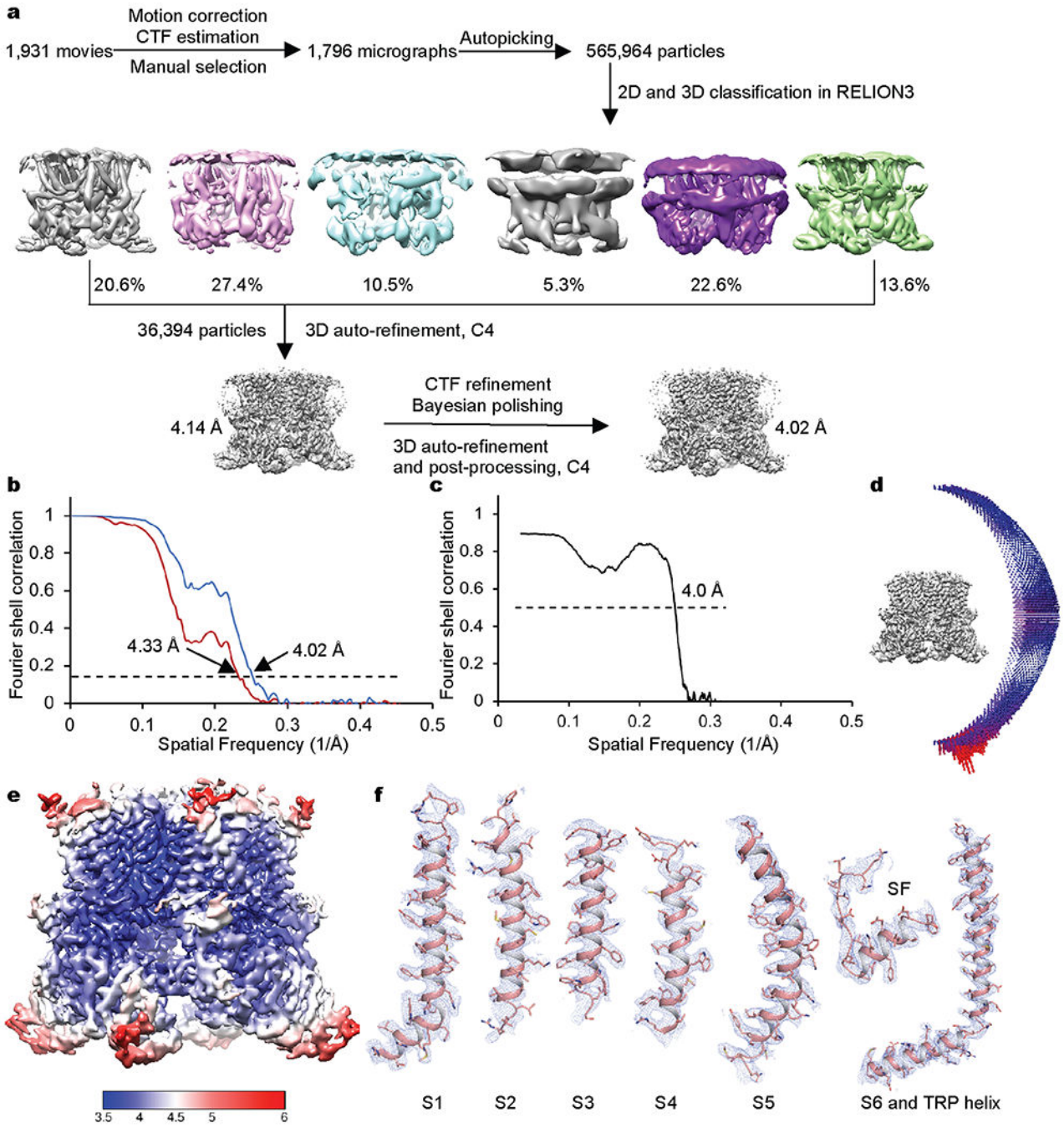


**Extended Data Fig. 8: Cryo-EM reconstruction of K169A briefly exposed to 2-APB for 3 minutes in an open conformation.**

**a**, Flowchart of cryo-EM data processing. **b**, Fourier shell correlation before and after post-processing in RELION3. **c**, Fourier shell correlation between the refined model and the full map. **d**, Angular distribution plot of particles used for final reconstruction. **e**, Cryo-EM density map colored by local resolution. **f**, Representative cryo-EM density shown as blue mesh contoured at 5.0 σ.

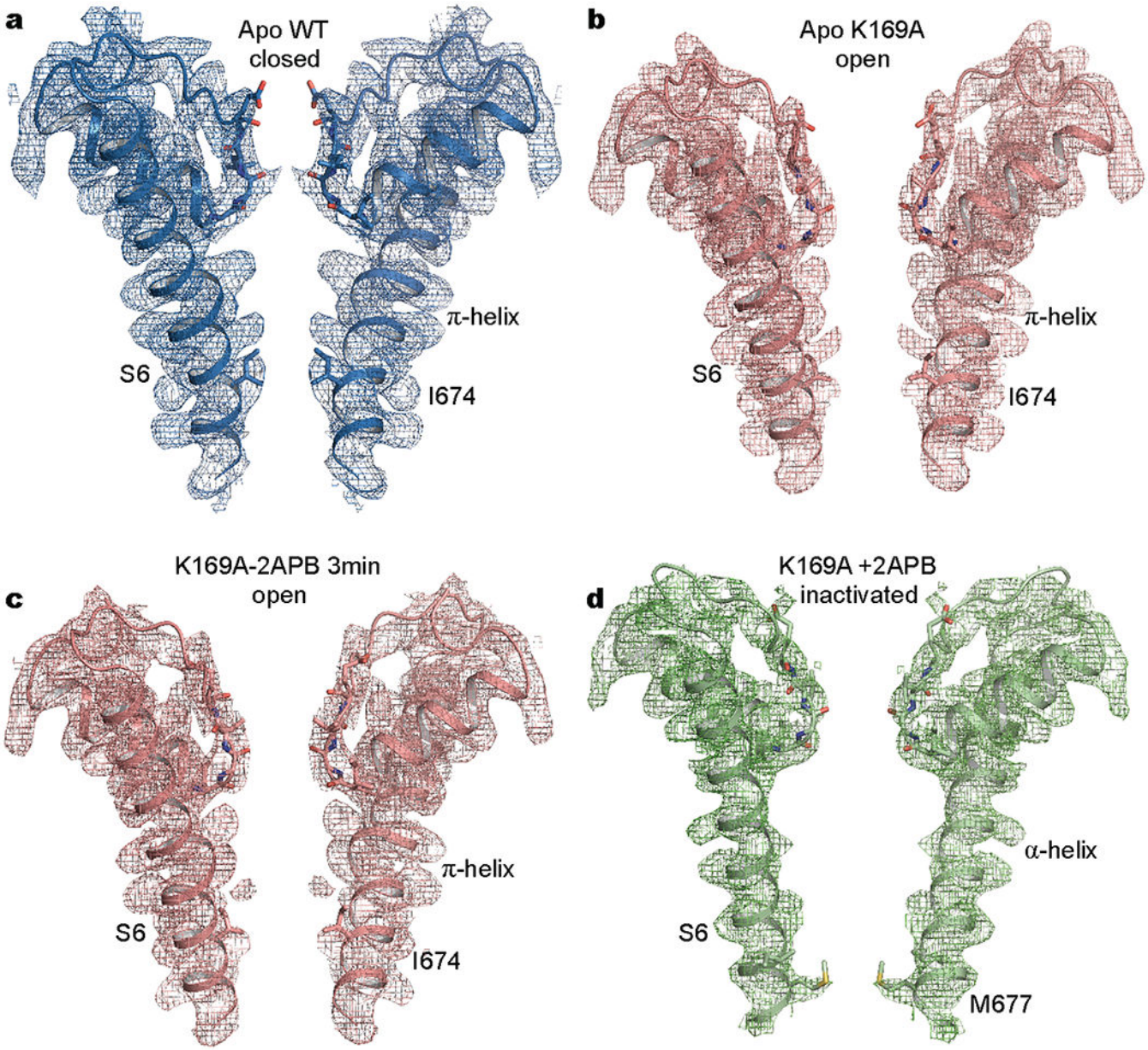


**Extended Data Fig. 9: TRPV3 pore structures in distinct functional states.**

**a-d**, The pore structures in the apo closed wild-type TRPV3 channel (**a**), the apo open K169 mutant (**b**), the 2-APB-bound open K169A (**c**), and 2-APB-bound inactivated states (**d**). Also shown are cryo-EM densities of the normalized cryo-EM maps contoured at 6.0 σ.

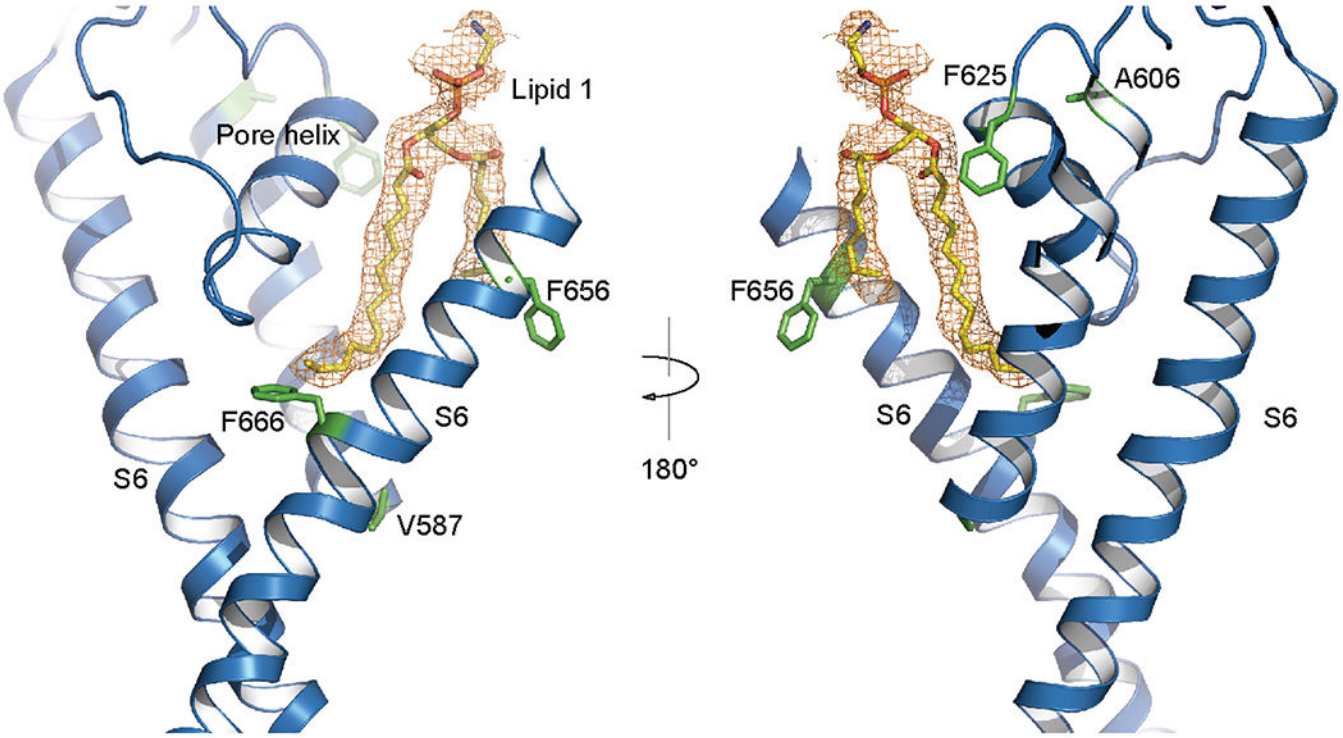


**Extended Data Fig. 10: Mapping the pore mutations enabling TRPV3-6M activation by RTX.**
Two views of the closed TRPV3 pore, highlighting the pore mutations that render TRPV3-6M sensitive to RTX activation. These mutations, including V587L, A606V, F625L, F656I, and F666Y, are shown as stick representation and colored in green.

## Acknowledgements

This work was supported by National Institutes of Health Grant R01NS099341 and the Mallinckrodt Foundation grant (to P.Y.), and by the McDonnell Center for Cellular and Molecular Neurobiology Postdoctoral Fellowship (to Z.D.). M.R and J.A.J.F are supported by the Washington University Center for Cellular Imaging, which is funded, in part by Washington University School of Medicine through the Precision Medicine Initiative, the Children's Discovery Institute of Washington University and St. Louis Children's Hospital (CDI-CORE-2015-505 and CDI-CORE-2019-813) and the Foundation for Barnes-Jewish Hospital (3770).

## References

1. Clapham DE TRP channels as cellular sensors. Nature 426, 517–524 (2003). [PubMed: 14654832]
2. Ramsey IS, Delling M & Clapham DE An introduction to TRP channels. Annu. Rev. Physiol. 68, 619–647 (2006). [PubMed: 16460286]
3. Julius D TRP channels and pain. Annu. Rev. Cell Dev. Biol. 29, 355–384 (2013). [PubMed: 24099085]
4. Xu H et al. TRPV3 is a calcium-permeable temperature-sensitive cation channel. Nature 418, 181–186 (2002). [PubMed: 12077604]
5. Peier AM et al. A heat-sensitive TRP channel expressed in keratinocytes. Science 296, 2046–2049 (2002). [PubMed: 12016205]
6. Smith GD et al. TRPV3 is a temperature-sensitive vanilloid receptor-like protein. Nature 418, 186–190 (2002). [PubMed: 12077606]
7. Cheng X et al. TRP channel regulates EGFR signaling in hair morphogenesis and skin barrier formation. Cell 141, 331–343 (2010). [PubMed: 20403327]

8. Bang S, Yoo S, Yang TJ, Cho H & Hwang SW Farnesyl pyrophosphate is a novel pain-producing molecule via specific activation of TRPV3. J. Biol. Chem. 285, 19362–19371 (2010). [PubMed: 20395302]
9. Miyamoto T, Petrus MJ, Dubin AE & Patapoutian A TRPV3 regulates nitric oxide synthase-independent nitric oxide synthesis in the skin. Nat. Commun. 2, 369 (2011). [PubMed: 21712817]
10. Lin Z et al. Exome sequencing reveals mutations in TRPV3 as a cause of Olmsted syndrome. Am. J. Hum. Genet. 90, 558–564 (2012). [PubMed: 22405088]
11. Ni C et al. A novel mutation in TRPV3 gene causes atypical familial Olmsted syndrome. Sci. Rep. 6, 21815 (2016). [PubMed: 26902751]
12. Hu HZ et al. 2-Aminoethoxydiphenyl borate is a common activator of TRPV1, TRPV2, and TRPV3. J. Biol. Chem. 279, 35741–35748 (2004). [PubMed: 15194687]
13. Xu H, Delling M, Jun JC & Clapham DE Oregano, thyme and clove-derived flavors and skin sensitizers activate specific TRP channels. Nat. Neurosci. 9, 628–635 (2006). [PubMed: 16617338]
14. Moqrich A et al. Impaired thermosensation in mice lacking TRPV3, a heat and camphor sensor in the skin. Science 307, 1468–1472 (2005). [PubMed: 15746429]
15. Chung MK, Lee H, Mizuno A, Suzuki M & Caterina MJ 2-Aminoethoxydiphenyl borate activates and sensitizes the heat-gated ion channel TRPV3. J. Neurosci. 24, 5177–5182 (2004). [PubMed: 15175387]
16. Xiao R et al. Calcium plays a central role in the sensitization of TRPV3 channel to repetitive stimulations. J. Biol. Chem. 283, 6162–6174 (2008). [PubMed: 18178557]
17. Phelps CB, Wang RR, Choo SS & Gaudet R Differential regulation of TRPV1, TRPV3, and TRPV4 sensitivity through a conserved binding site on the ankyrin repeat domain. J. Biol. Chem. 285, 731–740 (2010). [PubMed: 19864432]
18. Singh AK, McGoldrick LL & Sobolevsky AI Structure and gating mechanism of the transient receptor potential channel TRPV3. Nat. Struct. Mol. Biol. 25, 805–813 (2018). [PubMed: 30127359]
19. Zubcevic L et al. Conformational ensemble of the human TRPV3 ion channel. Nat. Commun. 9, 4773 (2018). [PubMed: 30429472]
20. Zubcevic L, Borschel WF, Hsu AL, Borgnia MJ & Lee S-Y Regulatory switch at the cytoplasmic interface controls TRPV channel gating. Elife 8, (2019).
21. Singh AK et al. Structural basis of temperature sensation by the TRP channel TRPV3. Nat. Struct. Mol. Biol. 26, 994–998 (2019). [PubMed: 31636415]
22. Liao M, Cao E, Julius D & Cheng Y Structure of the TRPV1 ion channel determined by electron cryo-microscopy. Nature 504, 107–112 (2013). [PubMed: 24305160]
23. Cao E, Liao M, Cheng Y & Julius D TRPV1 structures in distinct conformations reveal activation mechanisms. Nature 504, 113–118 (2013). [PubMed: 24305161]
24. Zubcevic L et al. Cryo-electron microscopy structure of the TRPV2 ion channel. Nat. Struct. Mol. Biol. 23, 180–186 (2016). [PubMed: 26779611]
25. Deng Z et al. Cryo-EM and X-ray structures of TRPV4 reveal insight into ion permeation and gating mechanisms. Nat. Struct. Mol. Biol. 25, 252–260 (2018). [PubMed: 29483651]
26. Grandl J et al. Temperature-induced opening of TRPV1 ion channel is stabilized by the pore domain. Nat. Neurosci. 13, 708–14 (2010). [PubMed: 20414199]
27. Jordt SE, Tominaga M & Julius D Acid potentiation of the capsaicin receptor determined by a key extracellular site. Proc. Natl. Acad. Sci. U. S. A. 97, 8134–8139 (2000). [PubMed: 10859346]
28. Cui Y et al. Selective disruption of high sensitivity heat activation but not capsaicin activation of TRPV1 channels by pore turret mutations. J. Gen. Physiol. 139, 273–283 (2012). [PubMed: 22412190]
29. Bohlen CJ et al. A bivalent tarantula toxin activates the capsaicin receptor, TRPV1, by targeting the outer pore domain. Cell 141, 834–845 (2010). [PubMed: 20510930]
30. Myers BR, Bohlen CJ & Julius D A yeast genetic screen reveals a critical role for the pore helix domain in TRP channel gating. Neuron 58, 362–373 (2008). [PubMed: 18466747]

31. Yang F, Cui Y, Wang K & Zheng J Thermosensitive TRP channel pore turret is part of the temperature activation pathway. Proc. Natl. Acad. Sci. U. S. A. 107, 7083–7088 (2010). [PubMed: 20351268]
32. Jara-Oseguera A, Huffer KE & Swartz KJ The ion selectivity filter is not an activation gate in TRPV1-3 channels. Elife 8, (2019).
33. Grandl J et al. Pore region of TRPV3 ion channel is specifically required for heat activation. Nat. Neurosci. 11, 1007–1013 (2008). [PubMed: 19160498]
34. Kim SE, Patapoutian A & Grandl J Single residues in the outer pore of TRPV1 and TRPV3 have temperature-dependent conformations. PLoS One 8, e59593 (2013). [PubMed: 23555720]
35. Hille B, Dickson EJ, Kruse M, Vivas O & Suh BC Phosphoinositides regulate ion channels. Biochim. Biophys. Acta - Mol. Cell Biol. Lipids 1851, 844–856 (2015).
36. Gao Y, Cao E, Julius D & Cheng Y TRPV1 structures in nanodiscs reveal mechanisms of ligand and lipid action. Nature 534, 347–351 (2016). [PubMed: 27281200]
37. Denisov IG & Sligar SG Nanodiscs for structural and functional studies of membrane proteins. Nat. Struct. Mol. Biol. 23, 481–486 (2016). [PubMed: 27273631]
38. Dang S et al. Cryo-EM structures of the TMEM16A calciumactivated chloride channel. Nature 552, 426–429 (2017). [PubMed: 29236684]
39. Kern DM, Oh S, Hite RK & Brohawn SG Cryo-EM structures of the DCPIB-inhibited volume-regulated anion channel LRRC8A in lipid nanodiscs. Elife 8, (2019).
40. Doerner JF, Hatt H & Ramsey IS Voltage- and temperature-dependent activation of TRPV3 channels is potentiated by receptor-mediated PI(4,5)P 2 hydrolysis. J. Gen. Physiol. 137, 271–288 (2011). [PubMed: 21321070]
41. Bang S, Yoo S, Yang TJ, Cho H & Hwang S 17(R)-resolvin D1 specifically inhibits transient receptor potential ion channel vanilloid 3 leading to peripheral antinociception. Br. J. Pharmacol. 165, 683–692 (2012). [PubMed: 21718307]
42. Hu HZ et al. Potentiation of TRPV3 channel function by unsaturated fatty acids. J. Cell. Physiol. 208, 201–212 (2006). [PubMed: 16557504]
43. Hughes TET et al. Structural insights on TRPV5 gating by endogenous modulators. Nat. Commun. 9, 4198 (2018). [PubMed: 30305626]
44. Saotome K, Singh AK, Yelshanskaya MV & Sobolevsky AI Crystal structure of the epithelial calcium channel TRPV6. Nature 534, 506–511 (2016). [PubMed: 27296226]
45. McGoldrick LL et al. Opening of the human epithelial calcium channel TRPV6. Nature 553, 233–237 (2018). [PubMed: 29258289]
46. Long SB, Tao X, Campbell EB & MacKinnon R Atomic structure of a voltage-dependent K+ channel in a lipid membrane-like environment. Nature 450, 376–382 (2007). [PubMed: 18004376]
47. Dang S et al. Structural insight into TRPV5 channel function and modulation. Proc. Natl. Acad. Sci. U. S. A. 116, 1–27 (2019).
48. Chung MK, Güler AD & Caterina MJ Biphasic currents evoked by chemical or thermal activation of the heat-gated ion channel, TRPV3. J. Biol. Chem. 280, 15928–15941 (2005). [PubMed: 15722340]
49. Luo J, Stewart R, Berdeaux R & Hu H Tonic inhibition of TRPV3 by Mg2+ in mouse epidermal keratinocytes. J. Invest. Dermatol. 132, 2158–2165 (2012). [PubMed: 22622423]
50. Cheng W et al. Heteromeric heat-sensitive transient receptor potential channels exhibit distinct temperature and chemical response. J. Biol. Chem. 287, 7279–7288 (2012). [PubMed: 22184123]
51. Palovcak E, Delemotte L, Klein ML & Carnevale V Comparative sequence analysis suggests a conserved gating mechanism for TRP channels. J. Gen. Physiol. 146, 37–50 (2015). [PubMed: 26078053]
52. Hinman a a, Chuang H. H. a B., Bautista D. M. a & Julius D. a. TRP channel activation by reversible covalent modification. Proc. Natl. Acad. Sci. U. S. A. 103, 19564–19568 (2006). [PubMed: 17164327]
53. Li M, Jiang J & Yue L Functional characterization of homo- and heteromeric channel kinases TRPM6 and TRPM7. J. Gen. Physiol. 127, 525–537 (2006). [PubMed: 16636202]

54. Lievremont JP, Bird GS & Putney JW Mechanism of inhibition of TRPC cation channels by 2-aminoethoxydiphenylborane. Mol. Pharmacol. 68, 758–762 (2005). [PubMed: 15933213]
55. Togashi K, Inada H & Tominaga M Inhibition of the transient receptor potential cation channel TRPM2 by 2-aminoethoxydiphenyl borate (2-APB). Br. J. Pharmacol. 153, 1324–1330 (2008). [PubMed: 18204483]
56. Singh AK, Saotome K, McGoldrick LL & Sobolevsky AI Structural bases of TRP channel TRPV6 allosteric modulation by 2-APB. Nat. Commun. 9, 2465 (2018). [PubMed: 29941865]
57. Liu B, Yao J, Zhu MX & Qin F Hysteresis of gating underlines sensitization of TRPV3 channels. J. Gen. Physiol. 138, 509–520 (2011). [PubMed: 22006988]
58. Yang F, Vu S, Yarov-Yarovoy V & Zheng J Rational design and validation of a vanilloid-sensitive TRPV2 ion channel. Proc. Natl. Acad. Sci. U. S. A. 113, E3657–E3666 (2016). [PubMed: 27298359]
59. Zhang F et al. Engineering vanilloid-sensitivity into the rat TRPV2 channel. Elife 5, (2016).
60. Zhang F, Swartz KJ & Jara-Oseguera A Conserved allosteric pathways for activation of TRPV3 revealed through engineering vanilloid-sensitivity. Elife 8, (2019).
61. Zheng SQ et al. MotionCor2: anisotropic correction of beam-induced motion for improved cryo-electron microscopy. Nat. Methods 14, 331–332 (2017). [PubMed: 28250466]
62. Zhang K Gctf: Real-time CTF determination and correction. J. Struct. Biol. 193, 1–12 (2016). [PubMed: 26592709]
63. Scheres SHW RELION: Implementation of a Bayesian approach to cryo-EM structure determination. J. Struct. Biol. 180, 519–530 (2012). [PubMed: 23000701]
64. Punjani A, Rubinstein JL, Fleet DJ & Brubaker MA CryoSPARC: Algorithms for rapid unsupervised cryo-EM structure determination. Nat. Methods 14, 290–296 (2017). [PubMed: 28165473]
65. Zivanov J et al. New tools for automated high-resolution cryo-EM structure determination in RELION-3. Elife 7, (2018).
66. Pettersen EF et al. UCSF Chimera--a visualization system for exploratory research and analysis. J. Comput. Chem. 25, 1605–1612 (2004). [PubMed: 15264254]
67. Emsley P, Lohkamp B, Scott WG & Cowtan K Features and development of Coot. Acta Crystallogr. D. Biol. Crystallogr 66, 486–501 (2010). [PubMed: 20383002]
68. Adams PD et al. PHENIX : a comprehensive Python-based system for macromolecular structure solution. Acta Crystallogr. D. Biol. Crystallogr 66, 213–221 (2010). [PubMed: 20124702]
69. Chen VB et al. MolProbity: All-atom structure validation for macromolecular crystallography. Acta Crystallogr. D. Biol. Crystallogr 66, 12–21 (2010). [PubMed: 20057044]
70. Schnorf M, Potrykus I & Neuhaus G Microinjection technique: routine system for characterization of microcapillaries by bubble pressure measurement. Exp. Cell Res. 210, 260–267 (1994). [PubMed: 8299724]

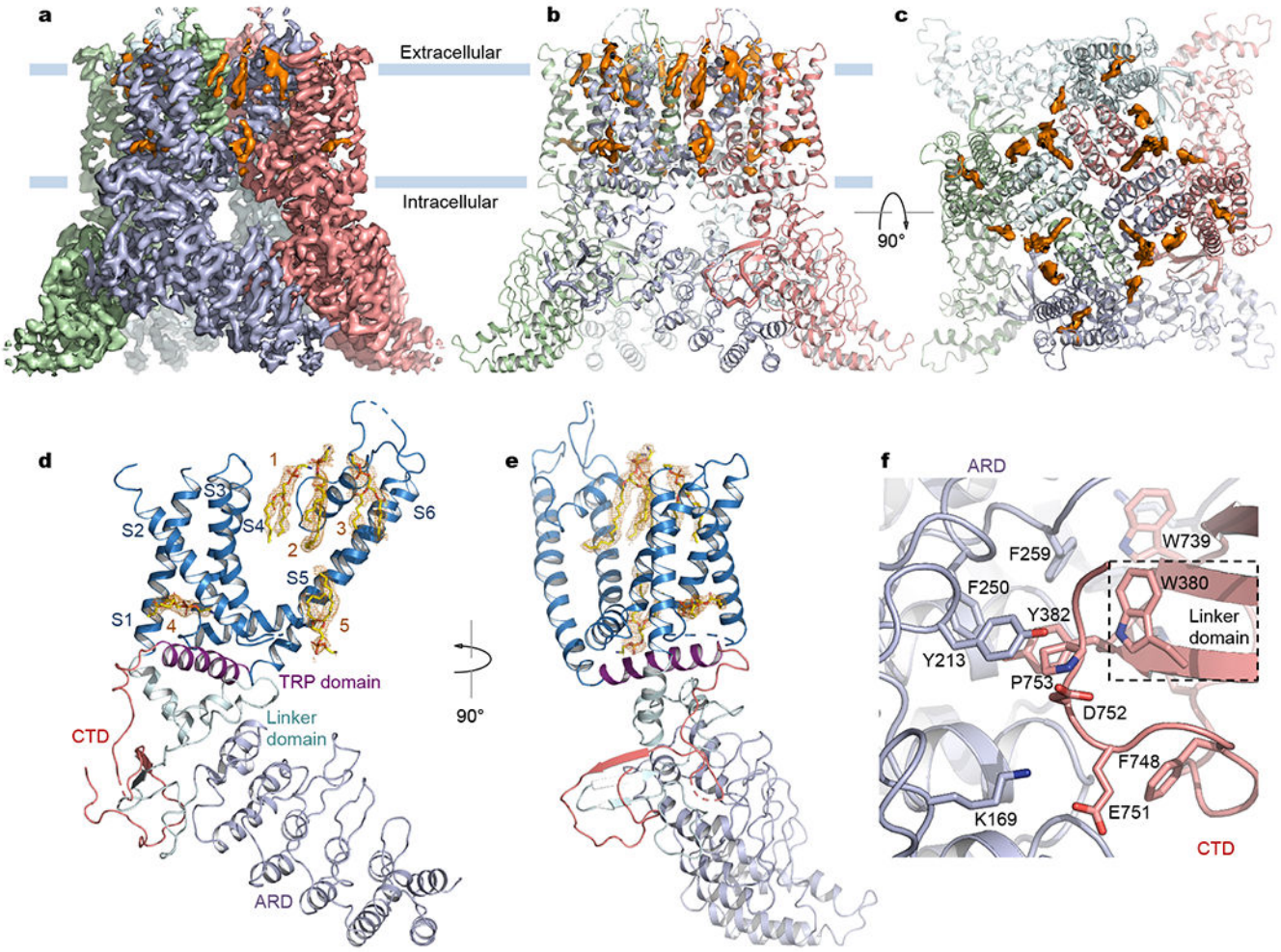


**Fig. 1 |. Cryo-EM structure of human TRPV3 in lipid nanodiscs.**

**a**, Cryo-EM reconstruction of the full-length wild-type human TRPV3 ion channel. The cryo-EM density is contoured at 6.0 σ. Each subunit is shown in a unique color and lipid densities are colored in brown. **b**,**c**, Orthogonal views of the TRPV3 structure. **d**,**e**, Two views of the structure of a single subunit with putatively bound lipids at sites 1-5. The lipid densities, shown as brown mesh contoured at 3.5 σ, can be well fitted with phospholipids such as phosphatidylethanolamine to illustrate the positions of the head groups and acyl chains. **f**, Cytoplasmic inter-subunit interface mediated by the linker domain, CTD, and ARD from an adjacent subunit. Residues at the interface are highlighted in stick representation.

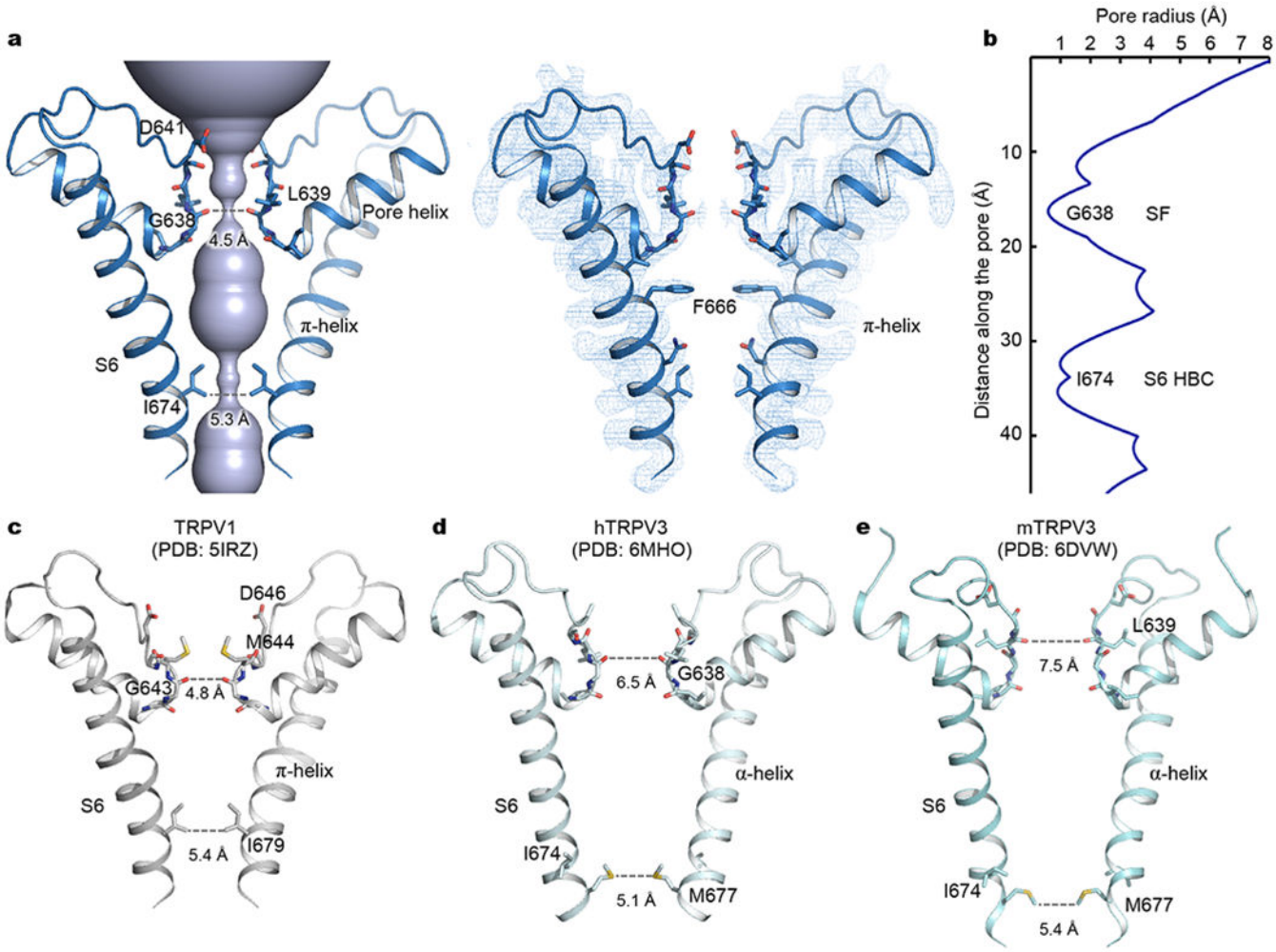


**Fig. 2 |. Two physical constrictions along the ion pore of TRPV3 in a lipid bilayer.**

**a**, The ion conduction pore of TRPV3 in a lipid bilayer, shown as light blue surface calculated with the program HOLE. The front and back subunits are removed for clarity. Two narrow constrictions at the selectivity filter and the intracellular S6 bundle-crossing regions are illustrated. The cryo-EM density in the pore region, contoured at 6.0 **σ**, is shown on the right. **b**, Dimension of the ion conduction pore. **c**, The pore structure of TRPV1 in the closed state (PDB: 5IRZ). **d**,**e**, The pore structures of human TRPV3 in amphipols (**d**, PDB: 6MHO) and mouse TRPV3 in detergents (**e**, PDB: 6DVW) in the apo states.

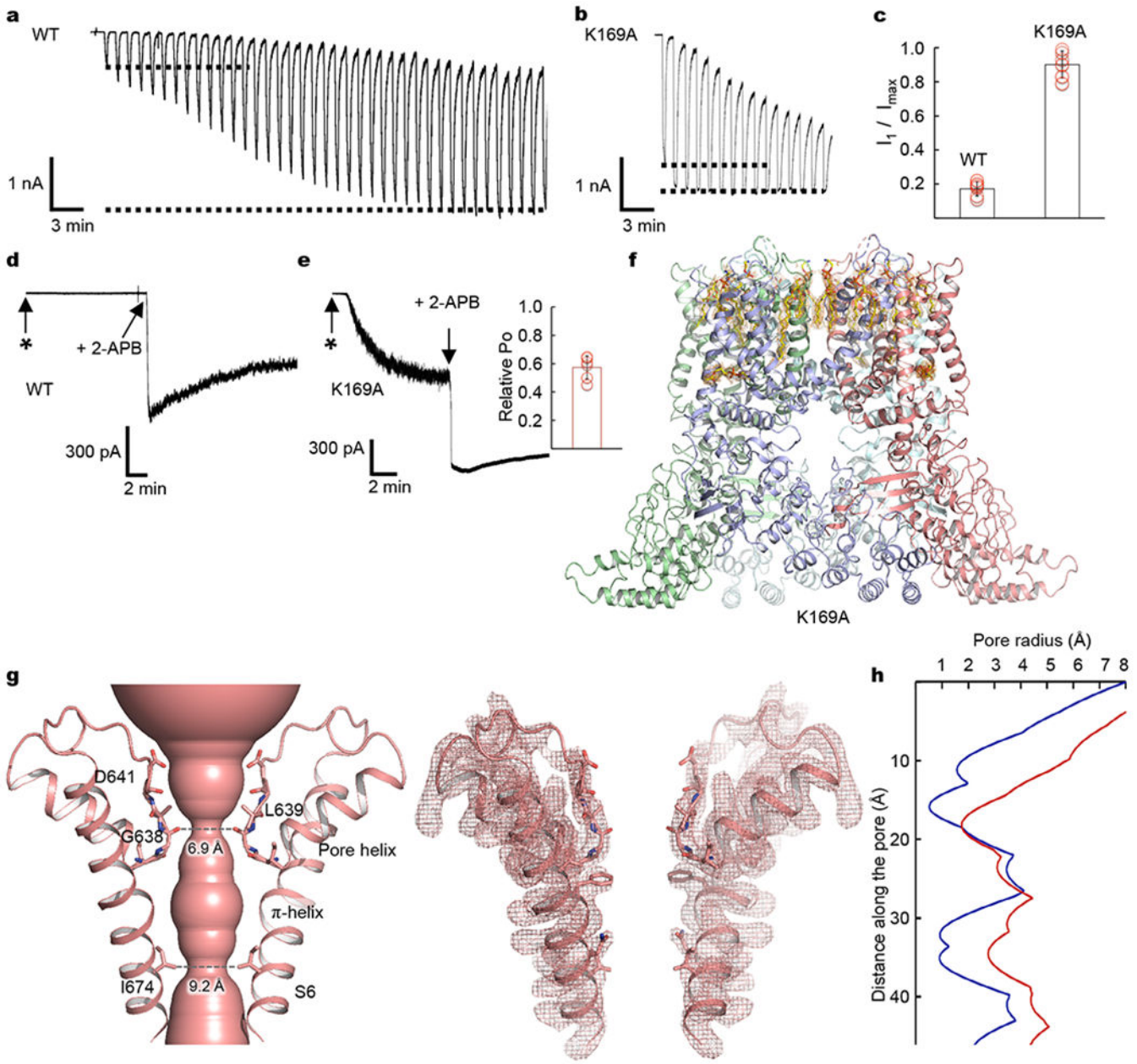


**Fig. 3 |. TRPV3 opening in a lipid bilayer.**

**a**,**b**, The wild-type TRPV3 (**a**) and K169A (**b**) currents in an inside-out membrane patch elicited by repetitive application of 30 μM 2-APB at −30 mV. **c**, Ratios of the first round of current response to the maximal response for the wild type (0.17 ± 0.04, n = 6) and K169A (0.90 ± 0.08, n = 6) (MEAN ± STDDEV, n independent biological experiments). **d**, **e**, Basal currents of the wild-type TRPV3 (**d**) and K169A (**e**) at −20 mV. Asterisk indicates patch excision. 2-APB (300μM) was added 10 minutes following patch excision. The K169A channels spontaneously open upon patch excision while the wild-type channels remain silent without application of 2-APB. The relative basal open probability of K169A, indicated by the current ratio in the absence to presence of 2-APB, is 0.57 ± 0.08 (6 independent

biological experiments). **f**, Open structure of the TRPV3 K169A mutant. Lipid densities are shown as orange mesh contoured at 3.5 σ. **g**, Ion conduction pore in the open conformation. Cryo-EM density contoured at 6.0 σ is shown on the right panel. **h**, Comparison of the dimensions of the open and closed pores.

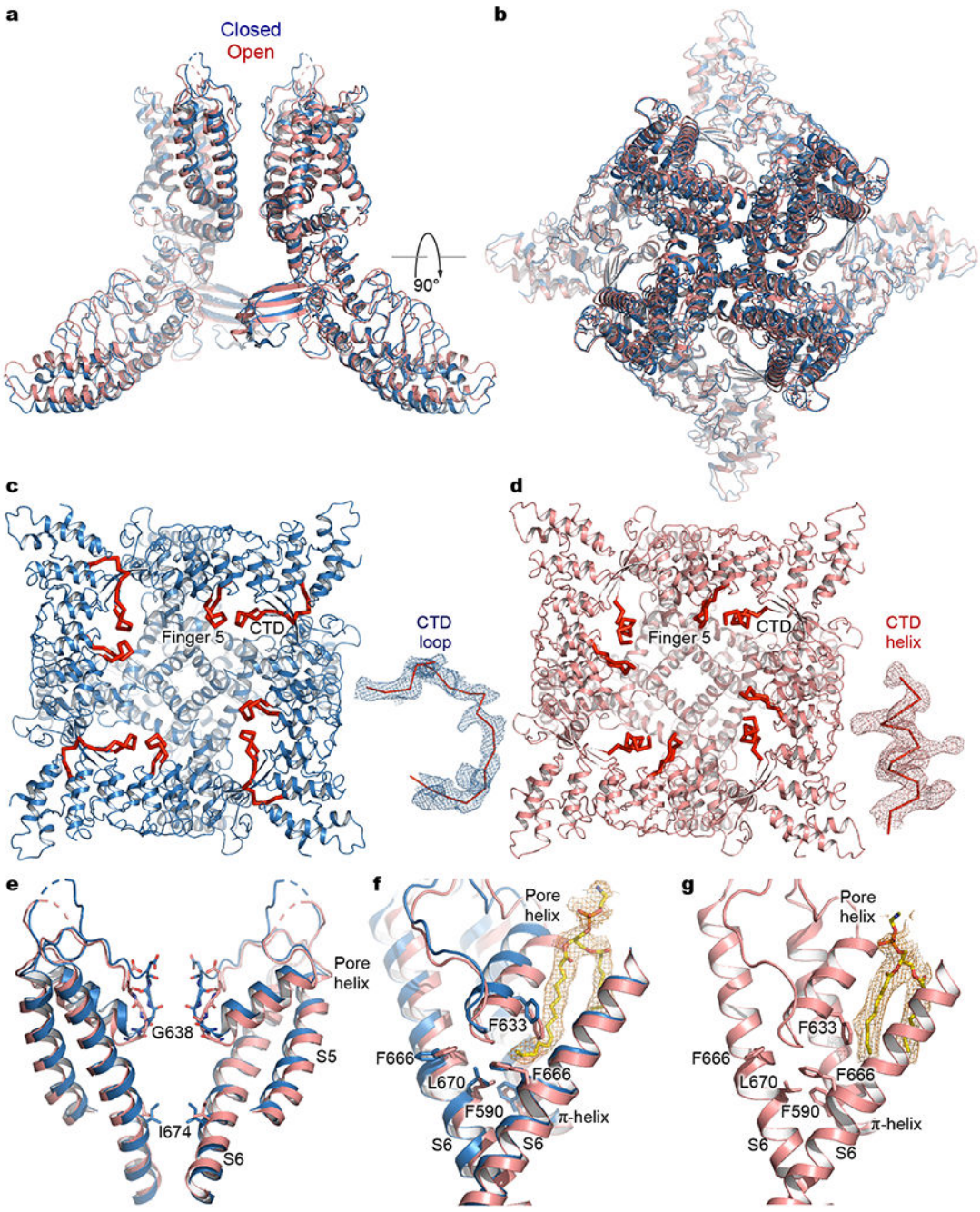


**Fig. 4 |. Conformational changes upon channel opening.**

**a**,**b**, Orthogonal views of superposition of the wild-type TRPV3 (closed) and K169A (open) structures. Structures are aligned using all four subunits. **c**,**d**, The distal CTD and finger 5 of the ARD in the closed (**c**) and open (**d**) conformations. Cryo-EM density contoured at 6.0 σ is also shown for the distal CTD. **e**, Superposition of the closed and open pores. **f**,**g**, Lipid at site 2 in the closed (**f**, blue) and open (**g**, red) conformations. Lipid densities are shown as brown mesh at 3.0 σ. Also shown in (**f**, red) is the aligned open pore to illustrate steric hindrance between the lipid and pore helix upon channel opening.

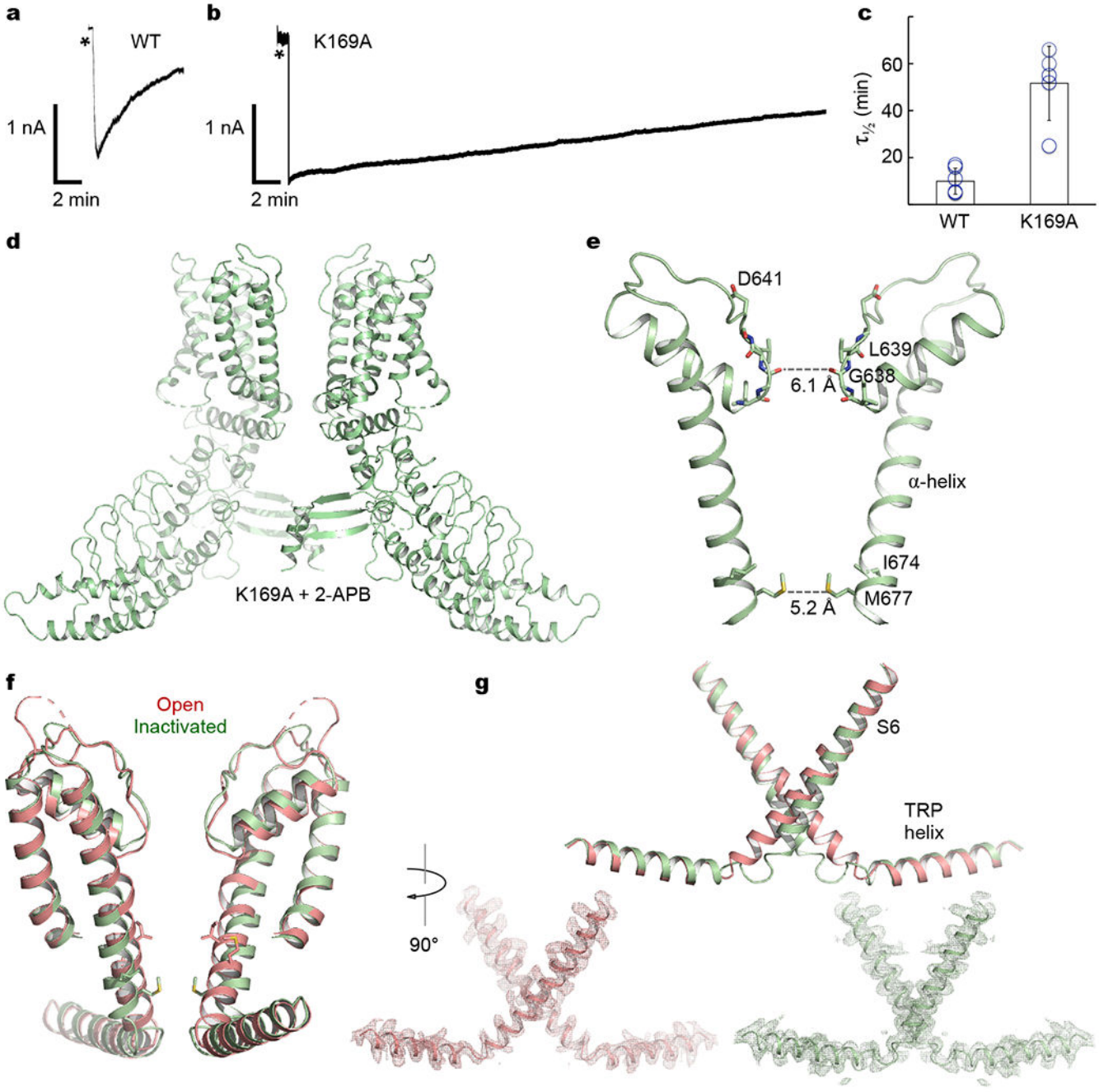


**Fig. 5 |. Structure of an inactivated conformation.**

**a**,**b**, The wild-type TRPV3 (**a**) and K169A (**b**) currents in an inside-out membrane patch induced by 1 mM 2-APB (indicated by asterisks) at −30 mV. The agonist was present in bath solutions during the entire course of recordings. **c**, Time for current decay to half maximum for the wild type (10.0 ± 5.5 min, n = 6) and K169A (51.6 ± 15.8 min, n = 5) (MEAN ± STDDEV, n independent biological experiments). **d**, Structure of K169A in the presence of 2-APB in an inactivated state. **e**, The ion conduction pore. The pore-lining helix S6 is α-helical and M677 lines the HBC gate. **f**, Superposition of the open and inactivated pores. **g**,

Comparison of the S6 and TRP helices in the open (red) and inactivated (green) structures. Also shown are cryo-EM densities for S6 and TRP helices in the open (red) and inactivated (green) states.

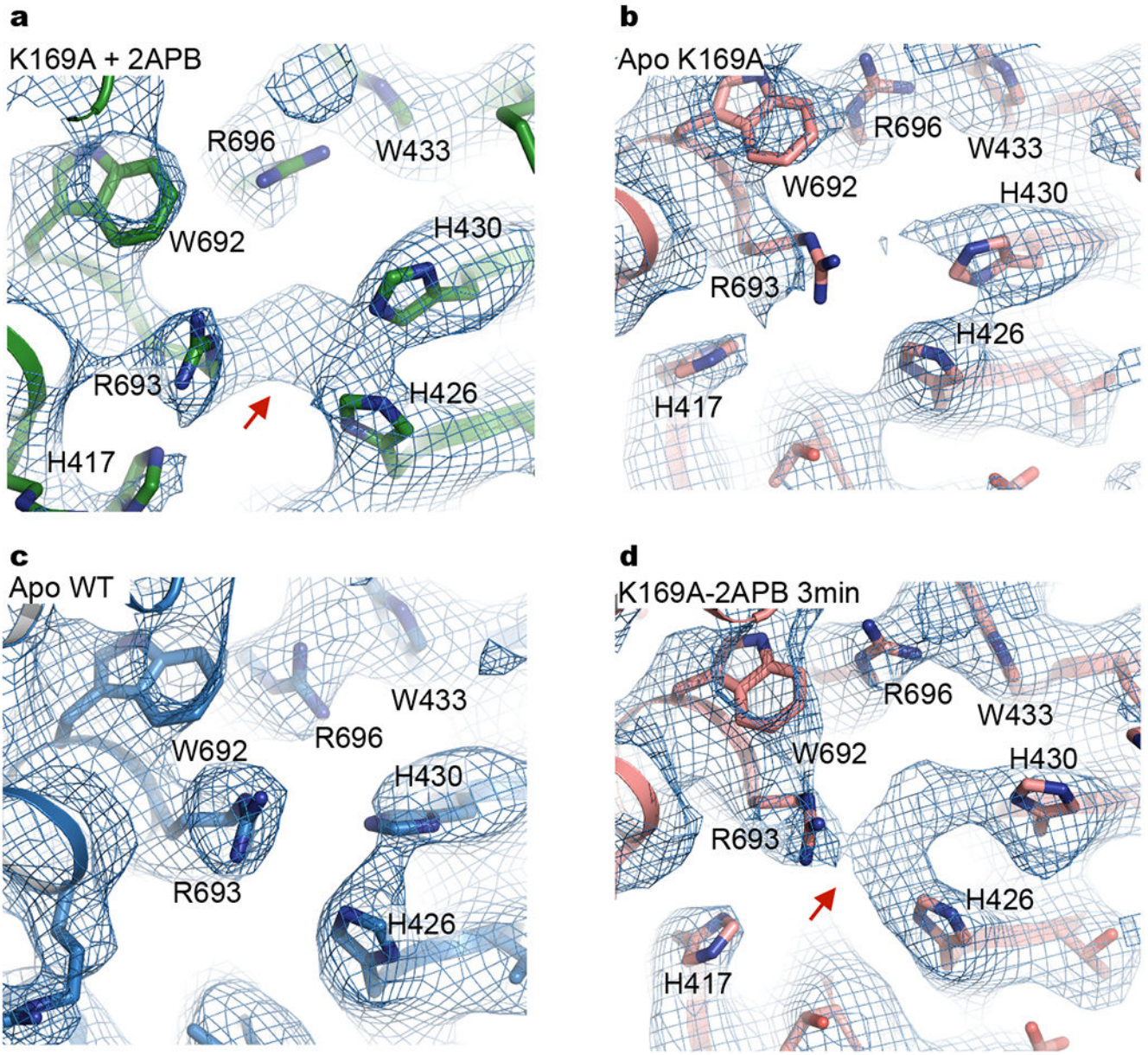


**Fig. 6 |. 2-APB binding site.**

**a-d**, Cryo-EM density in the 2-APB binding site in the 2-APB-bound inactivated (**a**), ligand-free open (**b**), ligand-free closed (**c**), and 2-APB-bound open states (**d**). Densities of normalized cryo-EM maps are shown as blue mesh contoured at 5.0 σ. The red arrow indicates the cryo-EM density attributable to 2-APB.

**Table 1 |**

Cryo-EM data collection, refinement and validation statistics

| | TRPV3 (EMD-20917, PDB 6UW4) | K169A (EMD-20918, PDB 6UW6) | K169A (2-APB, 3 min) (EMD-20919, PDB 6UW8) | K169+2-APB (EMD-20920, PDB 6UW9) |
|---|---|---|---|---|
| **Data collection and processing** | | | | |
| Magnification | 105,000 | 105,000 | 105,000 | 105,000 |
| Voltage (kV) | 300 | 300 | 300 | 300 |
| Electron exposure ($e^{-}$/Å$^2$) | 62 | 62 | 62 | 62 |
| Defocus range (μm) | −1.0 to −2.5 | −1.0 to −2.5 | −1.0 to −2.5 | −1.0 to −2.5 |
| Pixel size (Å) | 1.1 | 1.1 | 1.1 | 1.1 |
| Symmetry imposed | *C4* | *C4* | *C4* | *C4* |
| Initial particle images (no.) | 371,795 | 357,362 | 565,964 | 769,323 |
| Final particle images (no.) | 70,711 | 85,510 | 36,394 | 66,293 |
| Map resolution (Å) | 3.13 | 3.66 | 4.02 | 4.33 |
| FSC threshold | 0.143 | 0.143 | 0.143 | 0.143 |
| Map resolution range (Å) | 3.0-6.0 | 3.0-6.0 | 3.5-6.0 | 3.5-6.0 |
| **Refinement** | | | | |
| Initial model used | PDB 4N5Q | This study | This study | This study |
| Model resolution (Å) | 3.20 | 3.70 | 4.00 | 4.30 |
| FSC threshold | 0.5 | 0.5 | 0.5 | 0.5 |
| Model resolution range (Å) | 3.10 | 3.60 | 3.80 | 4.10 |
| Map sharpening *B* factor (Å$^2$) | −104 | −116 | −109 | −176 |
| Model composition | | | | |
| Non-hydrogen atoms | 20,281 | 20,072 | 19,640 | 18,924 |
| Protein residues | 2,412 | 2,408 | 2,408 | 2,328 |
| Ligands | 21 | 20 | 0 | 0 |
| *B* factors (Å$^2$) | | | | |
| Protein | 67.0 | 35.2 | 84.4 | 72.3 |
| Ligand | 63.0 | 28.7 | 0 | 0 |
| R.m.s. deviations | | | | |
| Bond lengths (Å) | 0.006 | 0.009 | 0.005 | 0.005 |
| Bond angles (°) | 0.881 | 1.034 | 0.899 | 1.138 |
| **Validation** | | | | |
| MolProbity score | 1.57 | 1.81 | 1.65 | 1.91 |
| Clashscore | 3.97 | 5.68 | 4.55 | 8.17 |
| Poor rotamers (%) | 0 | 0 | 0 | 0.2 |
| Ramachandran plot | | | | |
| Favored (%) | 94.22 | 91.58 | 93.64 | 92.66 |
| Allowed (%) | 5.78 | 8.42 | 6.36 | 7.34 |
| Disallowed (%) | 0 | 0 | 0 | 0 |